Monthly Notices
of the
ROYAL ASTRONOMICAL SOCIETY

MNRAS **485,** 4024–4044 (2019)
Advance Access publication 2019 March 8

doi:10.1093/mnras/stz670

The SAMI Galaxy Survey: Bayesian inference for gas disc kinematics using a hierarchical Gaussian mixture model

Mathew R. Varidel,[1,2,3]★ Scott M. Croom,[1,2,3] Geraint F. Lewis,[1] Brendon J. Brewer,[4] Enrico M. Di Teodoro,[5] Joss Bland-Hawthorn,[1,3] Julia J. Bryant,[1,2,3,6] Christoph Federrath,[5] Caroline Foster,[1,3] Karl Glazebrook,[3,7] Michael Goodwin,[8] Brent Groves,[2,3,5] Andrew M. Hopkins,[9] Jon S. Lawrence,[9] Ángel R. López-Sánchez,[9,10] Anne M. Medling,[5,11]† Matt S. Owers,[10,12] Samuel N. Richards,[13] Richard Scalzo,[14] Nicholas Scott,[1,2,3] Sarah M. Sweet,[3,8] Dan S. Taranu[2,15,16] and Jesse van de Sande[1,3]

Affiliations are listed at the end of the paper

Accepted 2019 March 5. Received 2019 March 5; in original form 2019 January 17

ABSTRACT

We present a novel Bayesian method, referred to as BLOBBY3D, to infer gas kinematics that mitigates the effects of beam smearing for observations using integral field spectroscopy. The method is robust for regularly rotating galaxies despite substructure in the gas distribution. Modelling the gas substructure within the disc is achieved by using a hierarchical Gaussian mixture model. To account for beam smearing effects, we construct a modelled cube that is then convolved per wavelength slice by the seeing, before calculating the likelihood function. We show that our method can model complex gas substructure including clumps and spiral arms. We also show that kinematic asymmetries can be observed after beam smearing for regularly rotating galaxies with asymmetries only introduced in the spatial distribution of the gas. We present findings for our method applied to a sample of 20 star-forming galaxies from the SAMI Galaxy Survey. We estimate the global Hα gas velocity dispersion for our sample to be in the range $\bar{\sigma}_v \sim$[7, 30] km s^{-1}. The relative difference between our approach and estimates using the single Gaussian component fits per spaxel is $\Delta\bar{\sigma}_v/\bar{\sigma}_v = -0.29 \pm 0.18$ for the Hα flux-weighted mean velocity dispersion.

Key words: methods: data analysis – methods: statistical – techniques: imaging spectroscopy – galaxies: kinematics and dynamics.

1 INTRODUCTION

Accurately estimating the intrinsic gas kinematics is vital to answer specific science questions. For example, an open question remains about the drivers of turbulence within disc galaxies (e.g. Tamburro et al. 2009; Federrath et al. 2017a). There is much evidence for higher velocity dispersions in $z > 1$ galaxies compared to nearby galaxies (Genzel et al. 2006; Law et al. 2007; Förster Schreiber et al. 2009; Epinat et al. 2010; Wisnioski et al. 2011). While the physical drivers of turbulence are not well understood, possibilities include one or more of the following; unstable disc formation (Bournaud et al. 2010), Jeans collapse (Aumer et al. 2010), star formation feedback processes (Green et al. 2010, 2014), cold-gas accretion (Aumer et al. 2010), ongoing minor mergers (Bournaud, Elmegreen & Martig 2009), interactions between clumps (Dekel et al. 2009a; Dekel, Sari & Ceverino 2009b; Ceverino, Dekel & Bournaud 2010), interactions between clumps and spiral arms (Dobbs & Bonnell 2007), or interactions between clumps and the interstellar medium (Oliva-Altamirano et al. 2018).

To gain a better understanding of the drivers of gas turbulence within the disc, it is important to accurately determine the intrinsic velocity dispersion of the galaxy. However, a known issue of observations using spatially resolved spectroscopy is beam smearing. Beam smearing is the effect of spatially blurring the flux profile due to the atmospheric seeing. For observations using spectroscopy, beam smearing acts to spatially blend spectral features. The blending of spectral features at different line-of-sight (LoS)

★ E-mail: mathew.varidel@sydney.edu.au
† Hubble Fellow.

velocities acts to flatten the observed velocity gradient and increase the observed LoS velocity dispersion. For single-component disc models, this has been shown to greatly exacerbate the observed LoS velocity dispersion in the middle of the galaxy (Davies et al. 2011).

Several heuristic approaches have been used to estimate the intrinsic velocity dispersion of a galaxy. A popular approach is to estimate the velocity dispersion away from the centre of the galaxy (e.g. Johnson et al. 2018). Another approach is to apply corrections to the observed velocity dispersion as a function of properties that exacerbate the effect of beam smearing such as the seeing width and rotational velocity (Johnson et al. 2018). The local velocity gradient (Varidel et al. 2016) has also been used to ignore spaxels with high local velocity gradient (Federrath et al. 2017b; Zhou et al. 2017) as well as provide corrections for the global (Varidel et al. 2016) and local velocity dispersion (Oliva-Altamirano et al. 2018).

Forward modelling approaches have also been used to simultaneously model the flux and kinematic profiles. In these algorithms, a 3D modelled cube is constructed for the galaxy and then spatially convolved per spectral slice to simulate the effect of beam smearing. The convolved cube is compared to the observed data. In this way, the galaxy properties are fitted to the original data while accounting for the effects of beam smearing. There are several publicly available cube-fitting algorithms designed for optical observations known to the authors. Those are GALPAK3D (Bouché et al. 2015), GBKFIT (Bekiaris et al. 2016), and ^{3D}BAROLO (Di Teodoro & Fraternali 2015).

GALPAK3D and GBKFIT assume parametric radial flux and velocity profiles with constant velocity dispersion. These algorithms have been used to infer the intrinsic global velocity dispersion and bulk rotation properties (e.g. Contini et al. 2016; Oliva-Altamirano et al. 2018). However, due to the parametric construction of the galaxy models, the residuals often exhibit significant substructure. This will usually be dominated by the gas distribution as it often exhibits more complex structure than the idealized radial profiles.

An implementation of non-parametric radial profiles has been constructed in tilted ring models. These models decompose the galaxy into a series of rings each with independent flux and kinematic properties. Tilted ring models are appropriate for analysing galaxies that are well represented by non-parametric radial profiles. In particular, they produce exquisitely detailed non-parametric radial profiles for high-resolution data (e.g. fig. 4, Di Teodoro & Fraternali 2015).

A pioneering 3D tilted ring model was implemented in GALMOD (Sicking 1997) in the Gronigen Image Processing SYstem (GIPSY; van der Hulst et al. 1992). Examples of modern implementations of tilted-ring models are ^{3D}BAROLO and TIRIFIC. TIRIFIC has received considerable development allowing for increased flexibility on a standard tilted ring model. However, it has solely been used for H I radio observations. This is at least partially due it assuming the spectral dimension is frequency. While it would be possible to transform the optical wavelength dimension of the data to frequency for use in TIRIFIC, we are not aware of researchers that have used TIRIFIC on optical data. Instead, ^{3D}BAROLO has been used on both optical (e.g. Di Teodoro, Fraternali & Miller 2016; Di Teodoro et al. 2018) and radio observations (e.g. Iorio et al. 2017).

A typical assumption used in previous methods is that the gas substructure can be well modelled using a radial profile. However, the distribution of gas within a galaxy is often more complex including rings, spiral arms, or individual clumps. In this paper, we will outline a 3D method to model the gas distribution and kinematic profiles robustly despite substructure of the gas distribution within the disc. This algorithm is inspired by the works of Brewer et al. (2011b) and Brewer, Huijser & Lewis (2016), who modelled the photometry of lensed galaxies with substructure by decomposing galaxies into a number of blobs using mixture models of a positive definite basis function. Our method (referred to as BLOBBY3D) decomposes the gas distribution into a mixture model of a positive definite basis function while simultaneously fitting the gas kinematics. Our method assumes radial velocity and velocity dispersion profiles across the galaxy.

The outline of this paper is as follows. In Section 2 we will frame the inference problem in terms of Bayesian reasoning and describe the model parametrization. In Section 3 we will discuss applications of our method to several toy data sets. In Section 4 we will apply the method to a sample of galaxies from the Sydney Australian-Astronomical-Observatory Multi-object Integral Field Spectrograph (SAMI) Galaxy Survey. In Section 5 we will discuss the implications of our results. We then make our concluding statements in Section 6.

2 MODEL DESCRIPTION

The problem of inferring the underlying galaxy properties can be formulated within the Bayesian framework as an inference for the galaxy parameters ($\boldsymbol{G}$), convolution parameters from the seeing and instrumental broadening ($\boldsymbol{\Sigma}$), and any systematic effects ($\boldsymbol{S}$) given some data (D),

$$p(\boldsymbol{G}, \boldsymbol{\Sigma}, \boldsymbol{S}|\boldsymbol{D}) \propto p(\boldsymbol{G}, \boldsymbol{\Sigma}, \boldsymbol{S})p(\boldsymbol{D}|\boldsymbol{G}, \Sigma, \boldsymbol{S}) \tag{1}$$

$$\propto p(\boldsymbol{\Sigma})p(\boldsymbol{S}|\boldsymbol{\Sigma})p(\boldsymbol{G}|\boldsymbol{\Sigma}, \boldsymbol{S})p(\boldsymbol{D}|\boldsymbol{G}, \boldsymbol{\Sigma}, \boldsymbol{S}). \tag{2}$$

Bayes' theorem relates the inference for the parameters $\boldsymbol{G}$, , and $\boldsymbol{S}$ to our prior understanding in $p(\boldsymbol{G}, \boldsymbol{\Sigma}, \boldsymbol{S})$ and the data using the likelihood function, $p(\boldsymbol{D}|\boldsymbol{G}, \boldsymbol{\Sigma}, \boldsymbol{S})$. All galaxy inferences can be summarized in this way.

In this work, we will assume that the convolution parameters are known. That is, $p(\boldsymbol{\Sigma})$ is a delta function that peaks at the assumed convolution parameters. The point spread function (PSF), representing the seeing, is typically estimated by modelling stars that are observed at the same time as the galaxies. Whereas the instrumental broadening is estimated by taking calibrations of the spectrograph using arc frames. Assuming that the convolution parameters are known will probably result in narrower posterior distributions than if we propagated our uncertainty in the convolution parameters.

Furthermore, we only consider systematic effects that are independent of the galaxy parametrization. Making the above assumptions, we approximate the problem represented in equation (2) to,

$$p(\boldsymbol{G}, \boldsymbol{S}|\boldsymbol{D}, \boldsymbol{\Sigma}) \propto p(\boldsymbol{G}, \boldsymbol{S})p(\boldsymbol{D}|\boldsymbol{G}, \boldsymbol{\Sigma}, \boldsymbol{S}) \tag{3}$$

$$\propto p(\boldsymbol{G})p(\boldsymbol{S})p(\boldsymbol{D}|\boldsymbol{G}, \boldsymbol{\Sigma}, \boldsymbol{S}). \tag{4}$$

The following sections will outline the assumptions made about the parametrization of $\boldsymbol{G}$, $\boldsymbol{\Sigma}$, and $\boldsymbol{S}$.

2.1 Galaxy parametrization ($\boldsymbol{G}$)

Our choice of galaxy parametrization is constructed with the aim to model the gas distribution and kinematics for a wide range of

Table 1. The hyperparameters, parameters, and data (i.e. all of the quantities involved in the inference), along with the prior distributions for each quantity. Taken together, these specify the joint prior distribution for the hyperparameters, parameters, and data, from which we obtain the posterior distribution. Where parameters are assumed to be known we represent the prior as a Dirac delta function with a user-input defined as $\mathcal{U}$. The notation $T(a, b)$ (written after a probability distribution) denotes truncation to the interval $[a, b]$. `ImageWidth` and `PixelWidth` refer to the geometric mean of the spatial dimensions for the cube and a single pixel, respectively. Note that flux units are 10^{-16} erg s^{-1} cm^{-2}.

Quantity	Meaning	Prior
Galaxy coordinate system ($\boldsymbol{C}$)		
x_c	x-coordinate for centre of galaxy	Cauchy(`XImageCentre`, 0.1 × `ImageWidth`)$T(x_{\min}, x_{\max})$
y_c	y-coordinate for centre of galaxy	Cauchy(`YImageCentre`, 0.1 × `ImageWidth`)$T(y_{\min}, y_{\max})$
θ	Galaxy semimajor axis angle (anticlockwise w.r.t. east)	Uniform(0, 2π)
i	Galaxy inclination ($i = 0$ for face-on)	$\delta(i - \mathcal{U})$
Number of blobs		
N	Number of blobs comprising the galaxy	Loguniform$\{1, 2, ..., 300\}$
Blob hyperparameters ($\boldsymbol{\alpha}$)		
μ_r	Typical distance of blobs from (x_c, y_c)	Loguniform(0.03 arcsec, 30 arcsec)
μ_F	Typical flux of blobs	Loguniform(10^{-3}, 10^3)
σ_F	Deviation of log flux from μ_F	Loguniform(0.03, 3)
$W_{\max}$	Maximum width of blobs	Loguniform(`PixelWidth`, 30 arcsec)
$q_{\min}$	Cut-off axial ratio	Uniform(0.2, 1)
Blob parameters ($\boldsymbol{B}_j$)		
F_j	Integrated flux	Lognormal(μ_F, σ_F^2)
r_j	Distance of centre from (x_c, y_c)	Exponential(μ_r)
θ_j	Polar angle of centre w.r.t. θ	Uniform(0.0, 2π)
w_j	Width of blob	Loguniform(`PixelWidth`, $W_{\max}$)
q_j	Axial ratio ($q = b/a$)	Triangular($q_{\min}$, 1)
ϕ_j	Orientation angle (anticlockwise w.r.t. $\theta + \theta_j$)	Uniform(0, π)
Velocity profile parameters ($\boldsymbol{V}$)		
$v_{\rm sys}$	Systemic velocity	Cauchy(0 km s^{-1}, 30 km s^{-1}) T(−150 km s^{-1}, 150 km s^{-1})
v_c	Asymptotic velocity	Loguniform(40 km s^{-1}, 400 km s^{-1})
r_t	Turnover radius for velocity profile	Loguniform(0.03 arcsec, 30 arcsec)
γ_v	Shape parameter for velocity profile	Loguniform(1, 100)
β_v	Shape parameter for velocity profile	Uniform(−0.75, 0.75)
Velocity dispersion profile parameters ($\boldsymbol{\Sigma}_V$)		
$\sigma_{v,0}$	Velocity dispersion at the kinematic centre	Loguniform(1 km s^{-1}, 200 km s^{-1})
$\sigma_{v,1}$	Log velocity dispersion gradient	Normal(0, 0.2^2)
Convolution parameters ($\boldsymbol{\Sigma}$)		
$A_{k,\rm PSF}$	Weight for each Gaussian representing the PSF	$\delta(A_{k,\rm PSF} - \mathcal{U})$
FWHM$_{k,\rm PSF}$	Seeing FWHM for each Gaussian representing the PSF	δ(FWHM$_{k,\rm PSF} - \mathcal{U}$)
FWHM$_{\rm lsf}$	Instrumental broadening	δ(FWHM$_{\rm lsf} - \mathcal{U}$)
Systematic parameters ($\boldsymbol{S}$)		
σ_0	Constant Gaussian noise component	Loguniform(10^{-12}, 10)
Data ($\boldsymbol{D}$)		
D_{ijk}	Flux for each velocity bin	Normal(M_{ijk}, $\sigma^2_{\rm obs} + \sigma_0^2$)

regularly rotating galaxies. We parametrize the gas distribution with respect to a single emission line.

A simplistic prior assumption for the gas distribution of a galaxy is that it consists of an unknown number of gas clouds that are gravitationally bound. The gas distribution will be centred and rotate around a single kinematic centre. The velocity profile is assumed to be radial with a gradient that is steep near the kinematic centre and plateaus at increasing radius. The velocity dispersion profile is assumed to follow a smoothly varying radial profile across the galaxy.

We will now describe the parametrization of the above prior assumption in accordance with Bayes' theorem. Note that we also describe the joint prior distribution including the assumed constants, parameters, hyper-parameters, and data in Table 1.

2.1.1 The galaxy coordinate system

The galaxy coordinate system is described by a kinematic centre at (x_c, y_c), an inclination angle i, and the semimajor axis position angle θ. This describes a thin plane for the gas to lie in. The set of parameters required to define the coordinate system are referred to as $\boldsymbol{C}$. The prior distribution for each parameter is assumed to be independent such that,

$$p(\boldsymbol{C}) = p(x_c)p(y_c)p(i)p(\theta). \quad (5)$$

The kinematic centre of the galaxy is typically in the centre of the field of view (FoV). We weakly incorporate this information by placing a wide-tailed Cauchy distribution centred in the middle of the image with a full width at half-maximum (FWHM) of 0.1 ×

`ImageWidth`. `ImageWidth` is defined to be the geometric mean length of the FoV. The prior distribution for the kinematic centre is truncated such that it cannot lie outside of the FoV.

We assume that the kinematic position angle follows a uniform distribution in the range $\theta \in [0, 2\pi]$. The inclination angle is typically constrained by the observed morphology and the kinematic profiles. However, it is often not possible to observe the full extent of the galaxy in IFS surveys. For example, a typical galaxy observed in the SAMI Galaxy Survey, which we will be using to test our methodology, is observed out to $\sim 2R_e$, where R_e is the half-light radius. This limits our ability to infer the inclination from the observed gas distribution. The LoS kinematic profiles are known to be approximately degenerate for varying inclination angles as well (e.g. fig. 9, Glazebrook 2013). We did test our methodology with a uniform prior for the inclination angle in the range $i \in [0, \pi/2]$. However, when applying our methodology to the sample galaxies in Section 4, we found that the inferred inclination angle could differ significantly from the estimated inclination angle when converting the observed ellipticity to an inclination angle assuming a thin disc. With this in mind, we assume that the inclination can be estimated from previous observations of the same galaxy with a wider FoV. The inclination is then set as a constant. The inclination and kinematic position angle are incorporated into the LoS velocity profile and define a plane that the gas lies in.

Setting the inclination angle as a constant will have several implications for our inferences. The inferred posterior distributions will probably be narrower than if we incorporated our uncertainty of the inclination angle into our model parametrization. Also, the effect of beam smearing on kinematic properties is a function of the LoS velocity profile which is affected by the inclination angle assumption. As such, we will introduce a systematic bias when our assumptions about the inclination are incorrect.

2.1.2 *The spatial gas distribution*

To incorporate our prior understanding within the galaxy parametrization, we decomposed the gas distribution into a sum of positive definite basis functions. We use positive definite basis functions as the integrated flux of a gas cloud should always be positive. Decomposing the gas distribution into a sum of positive definite basis functions is an approach to model complex structures such as spirals, rings, and clumps that are observed in galaxies. We refer to each component as a 'blob'.

We do not claim that a single blob represents an individual gas cloud. This is due to the following:

(i) The resolution of the data in many IFS studies is typically too low to resolve individual gas clouds.

(ii) The choice of parametrization for the positive definite basis function will lead to more or less blobs. This is due to the shape of the blob not perfectly matching the individual gas cloud. As such, several blobs may be required to model the shape of the gas cloud.

There are cases where an individual blob or a set of blobs may be assigned a particular classification such as an individual clump, spiral arm, or ring. However, such processing of the model output must be performed by the user after the modelling has been completed. For the majority of cases, the individual blobs should be seen as nuisance parameters. The primary reason for using blobs is to construct a flexible model of the gas distribution, rather than to derive properties of individual gas clouds.

There have been previous 3D approaches that decomposed galaxies into a series of sources (i.e. clouds or blobs). An example of this are the Monte Carlo integration techniques used in tilted ring models such as GALMOD (Sicking 1997). In these algorithms, the 3D tilted ring model is integrated using Monte Carlo sampling of point sources within a ring with a given gas column density and kinematics. However, the primarily goal is not to derive the individual parameters of the clouds, but rather to perform the integration of the 3D tilted ring model.

An alternative flexible approach, which has been applied to lensing data, is to use pixelated flux profiles. In these models, each pixel has an independent flux value. The pixelated flux profile is often regularized such that the resulting profile is smooth (e.g. Suyu et al. 2006). The advantage of this approach is that it can theoretically model any flux distribution at the observed scale, prior to performing the convolution. The disadvantage of the pixelated approach is that the prior distribution assigns high prior probability to flux profiles that look like noise and the regularization approach typically does not enforce the flux to be positive definite (Brewer et al. 2011b). As such, we have chosen to use the approach of modelling the gas distribution using a sum of positive definite basis functions.

We chose a Gaussian basis function where the integrated flux for each blob is always positive. Using a Gaussian basis function to represent the spatial gas distribution is not the only possibility. For example, generic Sèrsic profiles and quadratic polynomials with negative curvature calculated where the flux is positive have been used to model lensed galaxies by Brewer et al. (2011b, 2016). Other parametrizations of positive definite functions would also be feasible.

Each blob is defined by a set of parameters $\boldsymbol{B}_j$ that describe its integrated flux (F_j), central position (r_j, θ_j) with respect to the galaxy centre (x_c, y_c) and semimajor axis position angle (θ), width (w_j), axial ratio ($q_j = b/a$), and orientation (ϕ_j) with respect to $\theta + \theta_j$. The spatial component of the blob flux is then,

$$F(x', y') = \frac{F_j}{2\pi w_j^2} \exp\left(-\frac{1}{2w_j^2}\left(q_j x'^2 + \frac{y'^2}{q_j} \right) \right). \quad (6)$$

The coordinate system (x', y') is transformed with respect to the galaxy coordinate system defined by $\boldsymbol{C} = \{x_c, y_c, i, \theta\}$ and subsequently rotated with respect to the blob orientation (ϕ_j). To construct the flux map in the original coordinate system (i.e. $F(x, y)$), we calculate the flux per spaxel in the rotated coordinates and sum the flux contribution for each blob.

The blob parameters F_j, r_j, w_j, and q_j are hierarchically constrained. Hierarchical Gaussian mixture models refer to models that are a sum of Gaussians where the Gaussian parameters are hierarchically constrained. For a hierarchical Gaussian mixture model, a joint prior is constructed for the Gaussian parameters $\{\boldsymbol{B}_j\}_{j=1}^N$ for N Gaussians conditional on a set of hyperparameters $\boldsymbol{\alpha}$ (i.e. the parameters for the prior distribution). The joint prior distribution for N Gaussians is then described as,

$$p(\boldsymbol{\alpha}, \{\boldsymbol{B}_j\}_{j=1}^N) = p(\boldsymbol{\alpha}) \prod_{j=1}^{N} p(\boldsymbol{B}_j|\boldsymbol{\alpha}), \quad (7)$$

where $p(\boldsymbol{\alpha})$ refers to the prior distribution for the hyperparameters. The prior distribution for the blob parameters $\boldsymbol{B}_j$ are dependent on the hyperparameters encoded in $p(\boldsymbol{B}_j|\boldsymbol{\alpha})$.

The number of Gaussians required to adequately model the gas distribution is unknown prior to performing the inference. We can explicitly incorporate this within the joint prior distribution such

that,

$$p(N, \boldsymbol{\alpha}, \{\boldsymbol{B}_j\}_{j=1}^{N}) = p(N)p(\boldsymbol{\alpha}|N)\prod_{j=1}^{N} p(\boldsymbol{B}_j|\boldsymbol{\alpha}, N) \quad (8)$$

$$= p(N)p(\boldsymbol{\alpha})\prod_{j=1}^{N} p(\boldsymbol{B}_j|\boldsymbol{\alpha}). \quad (9)$$

The last step assumes the hyperparameters ($\boldsymbol{\alpha}$) and blob parameters $\{\boldsymbol{B}_j\}_{j=1}^{N}$ are independent from the number of Gaussians (N). We defined the prior distribution for the number of blobs $p(N)$ to be a loguniform distribution in the range $\{1, 2, 3, ..., N_{\rm max}\}$. We have set $N_{\rm max} = 300$ for all examples in this paper. Given six parameters per blob and a potential for up to 300 blobs, the total number of parameters to describe the full set of Gaussians is between 6 and 1800.

Hierarchical Gaussian mixture models are preferred when the parameters for the Gaussians follow a prior distribution where the hyperparameters are unknown. In our case, the hyperparameters are descriptors for the distribution of blobs which are specific for the observed galaxy. In this way the galaxy shape, typical blob shape, and individual blob parameters are inferred simultaneously.

We assume the integrated flux of the blobs follows a lognormal distribution suggesting that the blob has a typical integrated flux (μ_F) and deviation (σ_F). The lognormal distribution also ensures the integrated flux is positive.

The distance of the blobs (r_j) is assumed to follow an exponential distribution from the kinematic centre (x_c, y_c). This imparts a typical distance μ_r from the kinematic centre which is fitted per galaxy.

The width of the blobs (w_j) is assumed to follow a loguniform distribution. The choice of a loguniform distribution is chosen to avoid imparting a typical scale length as both disc and clumpy features may be required to model a given galaxy. The minimum width is defined by the `PixelWidth` which is the geometric mean of the x and y dimensions for a pixel. Restricting the minimum width of the blobs has been incorporated for several reasons. It limits the problem of accurately integrating and spatially convolving blobs that are much smaller than the pixel width. It also limits the possibility of overfitting the gas substructure. The maximum width ($W_{\rm max}$) is a free hyperparameter that is fitted for the galaxy.

The typical axial ratio ($q_j = b/a$) for a blob is also unknown prior to performing the inference. We chose a right-angled triangular prior distribution for q_j of the form,

$$p(q_j) = \frac{2(q_j - q_{\rm min})}{(1 - q_{\rm min})^2}. \quad (10)$$

The hyperparameter $q_{\rm min}$ is the minimum axial ratio. This prior imparts a preference for circular Gaussians.

2.1.3 *The velocity profile*

In the spectral dimension, we assume a single Gaussian emission line component per spaxel. The mean position per spaxel describes the rotational velocity profile across the galaxy. We assumed a continuous velocity profile across the blobs with a mean LoS velocity defined by the Courteau (1997) empirical model,

$$v(r) = v_{\rm c}\frac{(1 + r_t/r)^{\beta}}{(1 + (r_t/r)^{\gamma})^{1/\gamma}}\sin(i)\cos(\theta) + v_{\rm sys}. \quad (11)$$

r is defined as the distance in the galaxy plane to the kinematic centre. $v_{\rm sys}$ is a systemic velocity term, v_c is the asymptotic velocity, and r_t is the turnover radius. β is a shape parameter that describes the gradient for $r > r_t$, where positive results in a decreasing velocity profile and negative results in a increasing profile. γ describes how sharply the velocity profile turns over. We refer to the set of parameters describing the velocity profile as $\boldsymbol{V}$.

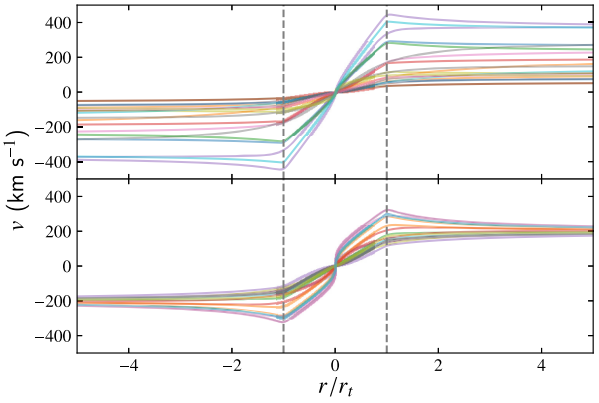

Figure 1. Prior samples of the radial velocity profile. Samples where all velocity parameters vary except $v_{\rm sys} = 0$ km s^{-1} (top) and with $v_c = 200$ km s^{-1} (bottom). Vertical lines indicate the turnover radius at $r = \pm r_t$. Our choice of priors for the velocity profile parameters were chosen to yield realistic radial velocity profiles.

The prior distribution for these parameters are assumed to be independent such that,

$$p(\boldsymbol{V}) = p(v_{\rm sys})p(v_c)p(r_t)p(\beta)p(\gamma). \quad (12)$$

It is assumed that the data cube is de-redshifted, but we allow for offsets for a non-zero systemic velocity by applying a prior that follows a wide-tailed Cauchy distribution with FWHM of 30 km s^{-1} and is truncated to the interval [−150 km s^{-1}, 150 km s^{-1}]. For all examples explored in this paper, the systemic velocity was well within these ranges. However, the range can be increased to account for a greater offsets if required.

The remaining parameters v_c, r_t, β, and γ are set with limits that yield a reasonable prior distribution by observing samples of the profiles. See Fig. 1 for velocity profiles using random samples from the prior for the velocity parameters. We assume loguniform prior for v_c in the range [40 km s^{-1}, 400 km s^{-1}]. The lower bound of 40 km s^{-1} for v_c was adequate for the test galaxies in this paper, but it can be easily lowered to take into account a larger sample of galaxies. The turnover radius (r_t) is assumed to follow a loguniform distribution in the range [0.03 arcsec, 30 arcsec].

Our velocity profile assumption yields a reasonably flexible radial profile, but we do not claim that this represents all galaxy velocity profiles. In particular, warps and asymmetries are not taken into account. Further flexibility may be required when the method is applied to larger data sets.

2.1.4 *The velocity dispersion profile*

The width of the Gaussian in the spectral dimension describes velocity dispersion per spaxel. The velocity dispersion profile is assumed to be a log-linear radial profile of the form,

$$\sigma_v(r) = \exp\left(\log(\sigma_{v,0}) + \sigma_{v,1}r\right), \quad (13)$$

where $\sigma_{v,0}$ represents the velocity dispersion at the kinematic centre (x_c, y_c) and $\sigma_{v,1}$ represents the log radial velocity dispersion gradient. We refer to the set of parameters that describe the galaxy velocity dispersion profile as $\boldsymbol{\Sigma_V}$. We used a log-linear profile such that $\sigma_v > 0$ at all radii. A disadvantage of this parametrization is that

for large $\sigma_{v,1}$, the observed σ_v can be much higher than is realistic. We use a normal prior distribution with mean 0 and variance 0.2^2 for $\sigma_{v,1}$ to limit unrealistically high-velocity dispersion gradients. We assume independence of the prior distributions for $\boldsymbol{\Sigma_V}$ such that,

$$p(\boldsymbol{\Sigma_V}) = p(\sigma_{v,0})p(\sigma_{v,1}). \quad (14)$$

During testing we also explored the possibility of having a single velocity dispersion per blob. While this would be ideal, it can lead to overfitting systematics that have not been corrected for appropriately. In particular, blobs with unrealistically high-velocity dispersion would often be required to account for systematic offsets in the continuum. This can occur in the log-linear model as well, but it is less affected due to the parametrization across the galaxy. Therefore, we have opted for a simplified parametric model which is more robust but less flexible.

2.1.5 *The full galaxy parametrization*

The flux distribution including a Gaussian instrumental broadening ($\sigma_{\rm lsf}$) within velocity space for a blob is defined as,

$$F(x, y, v) = \frac{F(x, y)}{\sqrt{2\pi(\sigma^2_{v(r(x,y))} + \sigma^2_{\rm lsf})}} \exp\left(\frac{(v - v(r(x, y)))^2}{\sqrt{\sigma^2_{v(r(x,y))} + \sigma^2_{\rm lsf}}}\right). \quad (15)$$

Equations (6), (11), (13), and (15) fully define the flux distribution of a blob for a given emission line for the spatial and velocity dimensions. The above model is converted from velocity to wavelength space such that the model can be compared to the data.

The full joint prior distribution for our galaxy model parametrization is described as,

$$p(\boldsymbol{G}) = p(\boldsymbol{C}, \boldsymbol{V}, \boldsymbol{\Sigma_V}, N, \boldsymbol{\alpha}, \{\boldsymbol{B}_j\}^N_{j=1}) \quad (16)$$

$$= p(\boldsymbol{C})p(\boldsymbol{V})p(\boldsymbol{\Sigma_V})p(N, \boldsymbol{\alpha}, \{\boldsymbol{B}_j\}^N_{j=1}) \quad (17)$$

$$= p(\boldsymbol{C})p(\boldsymbol{V})p(\boldsymbol{\Sigma_V})p(N)p(\boldsymbol{\alpha})\textstyle\prod^N_{j=1} p(\boldsymbol{B}_j|\boldsymbol{\alpha}). \quad (18)$$

The first step expands the galaxy parametrization ($\boldsymbol{G}$) to the sets of parameters describing the galaxy coordinate system ($\boldsymbol{C}$), velocity profile ($\boldsymbol{V}$), velocity dispersion profile ($\boldsymbol{\Sigma_V}$), number of blobs (N), the hyperparameters for the blobs ($\boldsymbol{\alpha}$), and the blob parameters ($\{\boldsymbol{B}_j\}^N_{j=1}$). The second step assumes independence between the various parameter sets where applicable. The third step expands the joint prior for N, $\boldsymbol{\alpha}$, and ($\{\boldsymbol{B}_j\}^N_{j=1}$) to state the dependence of the blob parameters ($\{\boldsymbol{B}_j\}^N_{j=1}$) on the blob hyperparameters ($\boldsymbol{\alpha}$) as in equation (9).

2.2 Sampling the prior for $\boldsymbol{G}$

The galaxy model parametrization is complex, including hierarchical constraints and a variable number of parameters dependent on the number of blobs. For such high-dimensional model parametrizations, it is often difficult to gain an intuitive understanding of the prior distribution. A common approach to check that a complex prior distribution is reasonable, is to visually check randomly drawn samples from the prior. As an example of this approach, we show 2D maps for 10 randomly drawn samples from the joint prior distribution in Fig. 2.

The 2D maps are constructed with a 15 arcsec and 0.5 arcsec square FoV and pixel width. These limits were constructed with the SAMI Galaxy Survey in mind, which has an FoV with typical diameter of ∼15 and 0.5 arcsec square pixels. We set the inclination $i = \pi/4$. For illustrative purposes, we also limit the prior samples shown in Fig. 2 such that $v_{\rm sys} \in [-10\,{\rm km\,s^{-1}}, 10\,{\rm km\,s^{-1}}]$ and x_c, y_c $\in [-3$ arcsec, 3 arcsec].

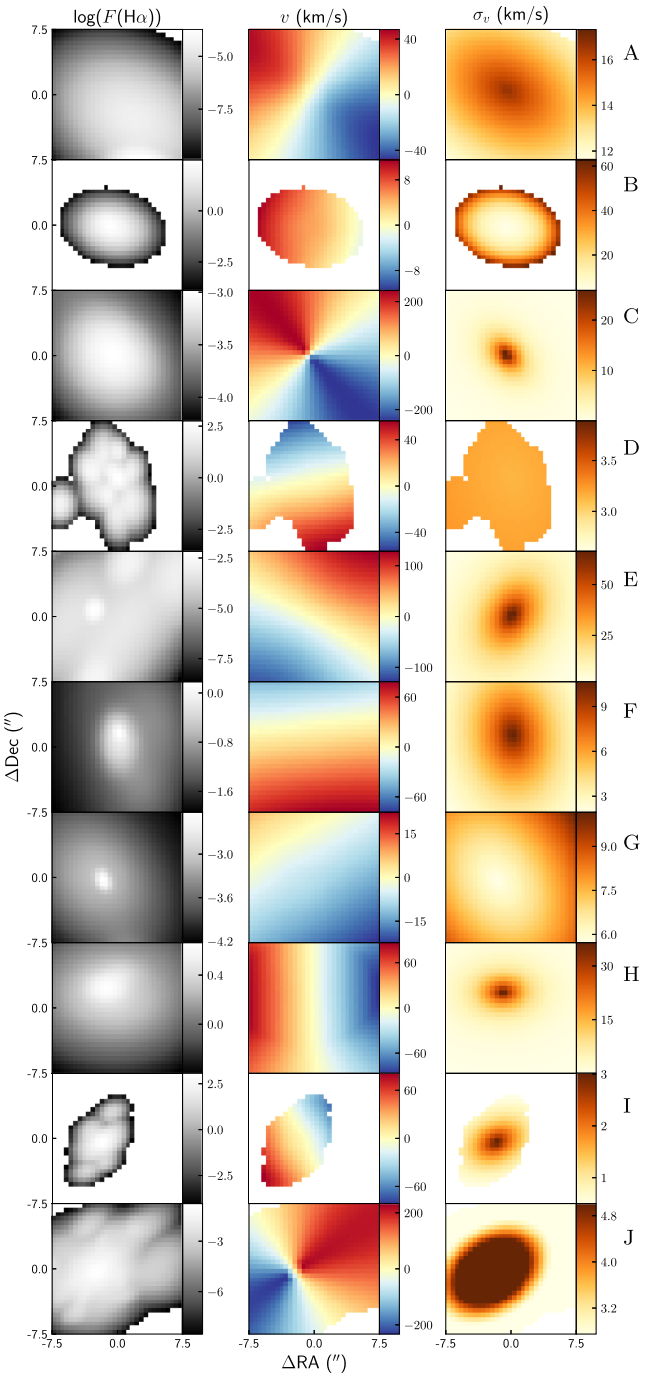

Figure 2. 2D maps of randomly drawn samples from the prior distribution for the Hα flux (left), LoS velocity (middle), and LoS velocity dispersion (right). For illustrative purposes, we show samples with inclination $i = \pi/4$, systemic velocity $v_{\rm sys} \in [-10\,{\rm km\,s^{-1}}, 10\,{\rm km\,s^{-1}}]$, and the kinematic centre $x_c, y_c \in [-3$ arcsec, 3 arcsec]. These maps show the flexibility of modelling the spatial gas distribution using a Gaussian mixture model. We also chose priors to yield realistic gas distributions and kinematic profiles.

In all samples there is a clear photometric and kinematic centre. These properties are constrained by the global parameters controlling the plane for the gas to lie in (i, θ) as well as the centre and typical distance for the blob centres (x_c, y_c, μ_r). Similarly, we avoid unusually shaped blobs by hierarchically constraining the width and axial ratio of the blobs.

Several samples add increased complexity with centralized peaks (e.g. F and G) and others with non-centralized clumps (e.g. D, E, F, I, J). The most unusual clump is probably in D on the west side of the image, but individual gas clumps similar to this are possible in real data (e.g. Richards et al. 2014).

The LoS velocity and velocity dispersion profiles are reasonable radial velocity profiles. Increased flexibility such as warps and asymmetries could be added to increase the realism of the profiles in the future.

We note that the prior distribution is a balance between flexibility and realism. As such, not all samples from the prior will represent realistic galaxies. Instead, the data are required to constrain the prior distribution via posterior sampling.

2.3 PSF convolution

The PSF convolution kernel is assumed to be well represented by a decomposition of concentric circular 2D Gaussians. Each Gaussian is described by $\mathbf{\Sigma}_k = \{A_{k,\,\mathrm{PSF}}, \mathrm{FWHM}_{k,\mathrm{PSF}}\}$ corresponding to the weight and FWHM for the k-th component. Each Gaussian has the separability property such that it can be deconstructed into two orthogonal vectors. Therefore, the 2D convolution is performed by convolving consecutively along each axis. Linear convolution using this method scales as $\mathcal{O}(N_{\mathrm{col,image}} N_{\mathrm{col,kern}} + N_{\mathrm{row,image}} N_{\mathrm{row,kern}})$ for each Gaussian. Further speed-up is gained by only constructing each Gaussian kernel out to $2.12 \times \mathrm{FWHM}_{\mathrm{PSF}}$, which is equivalent to $5\sigma_{\mathrm{PSF}}$.

Convolution is also a distributive operation. As such, we perform the convolution by each Gaussian component on the original image and then sum the convolved images. This method will scale linearly with the number of Gaussians required to model the kernel. We have only used 1–2 Gaussian components to represent the PSF as that was an acceptable number in our case.

In all examples in this paper, we have used representations of the kernel to be a Gaussian or Moffat profile. We do this as the pipeline for the SAMI Galaxy Survey provides estimates for the PSF for both the Gaussian and Moffat profiles. The PSF profile parameters are estimated by fitting observations of stars that have been taken simultaneously to observing the galaxies. In cases where the PSF is represented by a Moffat profile, we fit the 2D Moffat kernel with a sum of 2 Gaussians. The fitted parameters are then passed to the code implementation of our method.

2.4 Data

Our method assumes that the data cube has been isolated to a single emission line and the continuum has been subtracted. For optical IFS observations, this requires accurate modelling of the stellar continuum. In low signal-to-noise observations this may not be possible and thus signal-to-noise cuts of the data cube are required. While it may be ideal to parametrize the systematics in the continuum corrections, we avoided modelling the systematics to avoid introducing a high number of nuisance parameters to our model.

To isolate an emission line, typical optical IFS observations will need to be cut in the spectral dimension around the emission line of interest. This may be difficult in the spectral regions where there are multiple emission lines. In our examples, we will be focusing on the Hα emission line at 6562.8 Å which is adjacent to the two [N II] lines at 6548.1 and 6583.1 Å. Isolating the Hα emission line from the surrounding [N II] lines may be impossible for galaxies with high LoS velocity dispersions. In such cases, it will be a requirement to model the [N II] lines as this will cause systematics which we have not taken into account in our current parametrization. Adding the [N II] lines could be introduced to our method by modelling the [N II]/Hα per blob, then constraining the doublet using the theoretical ratio between the lines.

To construct the likelihood function, we assume the data follow a normal distribution. The mean is equal to an input data cube file $(D_{ijk,\mathrm{obs}})$. The variance is given by the sum of an input variance cube $(\sigma^2_{ijk,\mathrm{obs}})$ and an additional constant variance (σ_0^2),

$$\sigma^2_{ijk} = \sigma^2_{ijk,\mathrm{obs}} + \sigma_0^2, \tag{19}$$

σ_0^2 is a systematic noise parameter corresponding to $\boldsymbol{S}$ in our generic inference problem in equation (4). σ_0^2 helps take into account underestimated variance within the continuum subtracted data cube and some systematics that may arise due to limitations in the galaxy model parametrization. The additional variance term will not account for significant unresolved structures between the data and model. Under those circumstances, the posterior distributions can be systematically biased.

The non-diagonal elements of the covariance cube have not been incorporated. Including the non-diagonal elements of the covariance would require an inversion of the covariance matrix which scales as $\mathcal{O}(n^3)$. Data cubes cut around Hα typically have $\mathcal{O}(10^3)$ data points, which results in a highly time-consuming calculation. As such, we have avoided implementing the covariance matrix in the likelihood function. The likelihood function is then given by,

$$p(\boldsymbol{D}|\boldsymbol{G}, \mathbf{\Sigma}, \boldsymbol{S}) = \prod^{n_i}\prod^{n_j}\prod^{n_k} \frac{1}{\sqrt{2\pi\sigma^2_{ijk}}} \exp\left(-\frac{(M_{ijk} - D_{ijk})^2}{2\sigma^2_{ijk}}\right), \tag{20}$$

where M_{ijk} represents the model convolved by the PSF.

2.5 Posterior sampling

The posterior density function (PDF) is defined by equation (4), where the joint prior for the galaxy parametrization is given in equation (18), the prior for our systematic parameters is defined as $p(\boldsymbol{S}) = p(\sigma_0)$, and the likelihood function is given in equation (20). Table 1 also summarizes the joint prior distribution and data. The galaxy model is described by four global parameters, five blob hyperparameters, five velocity parameters, two velocity dispersion parameters, one systematic noise parameter, and six blob parameters for N blobs. For typical galaxies 10s–100s of blobs are required to sufficiently model the galaxy assuming our joint prior distribution. As such, the number of parameters required to model the galaxy is typically $\mathcal{O}(100)$, making this a high parameter model. It is also required to fit both the number of blobs as well as the parameters for those blobs.

With these requirements in mind, we use DNEST4 (Brewer, Pártay & Csányi 2011a; Brewer & Foreman-Mackey 2018). DNEST4 expands the nested sampling algorithm (Skilling 2004) by constructing future levels via a multilevel exploration of the posterior density function. The multilevel exploration is performed using an implementation of the Metropolis algorithm in the Markov-Chain

Monte Carlo class. DNEST4 is typically more robust to local maxima as it has the ability to walk up and down nested sampling levels to explore the posterior distribution. Furthermore, as DNEST4 is a nested sampling algorithm it can be used to calculate the evidence Z (i.e. the normalization constant for a given model), and subsequently perform model comparison.

DNEST4 also has an in-built reversible jump object (Brewer 2014). A reversible jump is a proposal step that allows for a change in components. We use this to propose steps that add or remove blobs such that we can perform posterior sampling for the number of blobs (N). An inference problem with a varying number of components is referred to as transdimensional inference. Such problems are notoriously difficult to explore, but DNEST4 has been used to successfully perform inferences on such problems as modelling lensed galaxies with a variable number of blobs (Brewer et al. 2011b, 2016), similar to our approach. Other applications within astronomy have been to estimate the number of stars in a crowded stellar field (Brewer, Foreman-Mackey & Hogg 2013) and modelling star formation histories (Walmswell et al. 2013).

3 TESTING THE METHOD

The remaining sections of this paper are devoted to demonstrating the methodology on a number of examples. We have tested the method on idealized toy models and real data. In this section, we will describe the applications of our method applied to a set of toy models.

3.1 Simple toy models

The toy models were constructed as a thin disc with an exponential flux profile. The velocity dispersion was set to a constant across the disc. We used an universal rotation curve (URC; Persic, Salucci & Stel 1996) to model the velocity profile.

The URC was chosen as this profile relates the flux profile to the velocity profile via the parameter $v(R_{\rm opt})$, where $R_{\rm opt}$ is equal to the 83 per cent-light radius. Another consideration in choosing the URC was to avoid using the same velocity profile in our toy models and our method. This way, we could test the ability of our method to infer the underlying kinematics despite having different velocity profile assumptions. The URC is defined as,

$$v(x) = \sqrt{v_d^2(x) + v_h^2(x)}, \tag{21}$$

where $v_d(x)$ and $v_h(x)$ represent the disc and halo velocity component contributions with $x = r/R_{\rm opt}$. The disc and halo components are defined as,

$$v_d^2(x) = v^2(R_{\rm opt})\beta \frac{1.97x^{1.22}}{(x^2 + 0.78^2)^{1.43}} \tag{22}$$

$$v_h^2(x) = v^2(R_{\rm opt})(1-\beta)(1+\alpha^2)\frac{x^2}{x^2+\alpha^2}, \tag{23}$$

where the shape parameters are

$$\alpha = 1.5\left(\frac{L}{L^*}\right)^{1/5} \quad \text{and} \quad \beta = 0.72 + 0.44\log_{10}\left(\frac{L}{L^*}\right). \tag{24}$$

We set $L/L* = 1$ for all toy models. A systemic velocity term was omitted for simplicity. The galaxies were inclined by 45° such that the LoS velocity was observable.

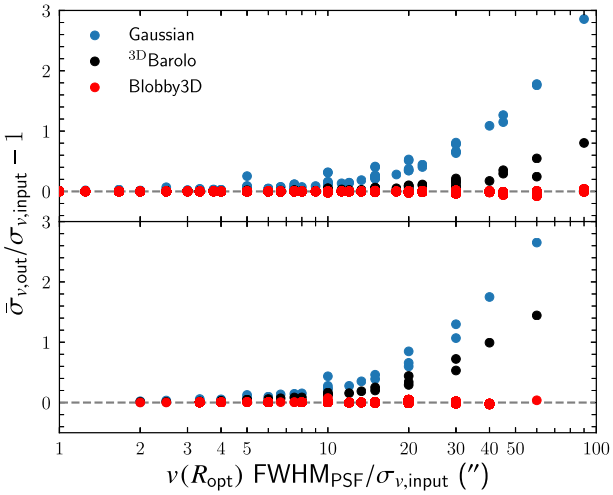

Figure 3. Relative difference between the estimated mean velocity dispersion ($\bar{\sigma}_{v,\rm out}$) and the input velocity dispersion ($\bar{\sigma}_{v,\rm input}$). This is shown as a function of $v(R_{\rm opt})$, the FWHM$_{\rm PSF}$, and the input velocity dispersion. The methods compared were a single-component Gaussian fit to each spaxel (blue), ^{3D}BAROLO (black), and our method (red). The model inputs are a grid of $\sigma_{v,\rm input} = \{10, 20, 30, 40, 50\}$ km s^{-1} and $v(R_{\rm opt}) = \{50, 100, 150, 200, 300\}$ km s^{-1}. The PSF profiles used are a Gaussian (top) with FWHM$_{\rm PSF}$ = {1 arcsec, 2 arcsec, 3 arcsec} and Moffat (bottom) with {FWHM$_{\rm PSF}$, $\beta_{\rm PSF}$} = {2 arcsec, 3}. Using the mean velocity dispersion after fitting a single-component Gaussian fit per spaxel, we found that the estimated velocity dispersion increased as a function of $v(R_{\rm opt})$FWHM$_{\rm PSF}/\sigma_{v,\rm input}$. ^{3D}BAROLO improves the estimates for the intrinsic mean velocity dispersion, yet still results in a trend similar to the estimates using the single-component Gaussian fit per spaxel. BLOBBY3D reliably infers the mean intrinsic velocity dispersion for our full grid of toy models.

The spatial edge of the cube was assumed set at 2 R_e. The cubes were oversampled by a factor of five elements in the spatial and wavelength directions. Emission lines were broadened by a Gaussian line-spread function (LSF) with FWHM$_{\rm LSF}$ = 1.61 Å similar to the SAMI Galaxy Survey (van de Sande et al. 2017) and convolved by the seeing per wavelength slice. The oversampled data cube was integrated to the desired resolution. The resulting cubes have a 15 arcsec × 15 arcsec FoV with 30 × 30 elements and a wavelength range of [6554 Å, 6571 Å] with 31 elements. The above choices were aimed at replicating a cube cut around the Hα emission line for a typical galaxy observed with the SAMI instrument (Croom et al. 2012).

To check for systematics in the kinematic inferences for different methods, we constructed the toy models with negligible noise. A grid of toy models was constructed with $\sigma_{v,\rm input} = \{10, 20, 30, 40, 50\}$ km s^{-1}, $v(R_{\rm opt}) = \{50, 100, 150, 200, 300\}$ km s^{-1}. The toy models were convolved with a Gaussian PSF with FWHM$_{\rm PSF}$ = {1 arcsec, 2 arcsec, 3 arcsec} or a Moffat PSF with {FWHM$_{\rm PSF}$, $\beta_{\rm PSF}$} = {2 arcsec, 3}.

3.1.1 *Estimating the velocity dispersion*

In Fig. 3, we show the relative difference between the estimated mean velocity dispersion ($\sigma_{v,\rm out}$) and the input velocity dispersion ($\sigma_{v,\rm input}$). The relative differences are shown compared to $v(R_{\rm opt})$FWHM$_{\rm PSF}/\sigma_{v,\rm input}$. This relationship yielded the clearest trend for the relative difference estimates using a single component Gaussian fit per spaxel. The intuitive reasoning for this relationship is that increasing $v(R_{\rm opt})/\sigma_{v,\rm input}$ increases the velocity gradient at

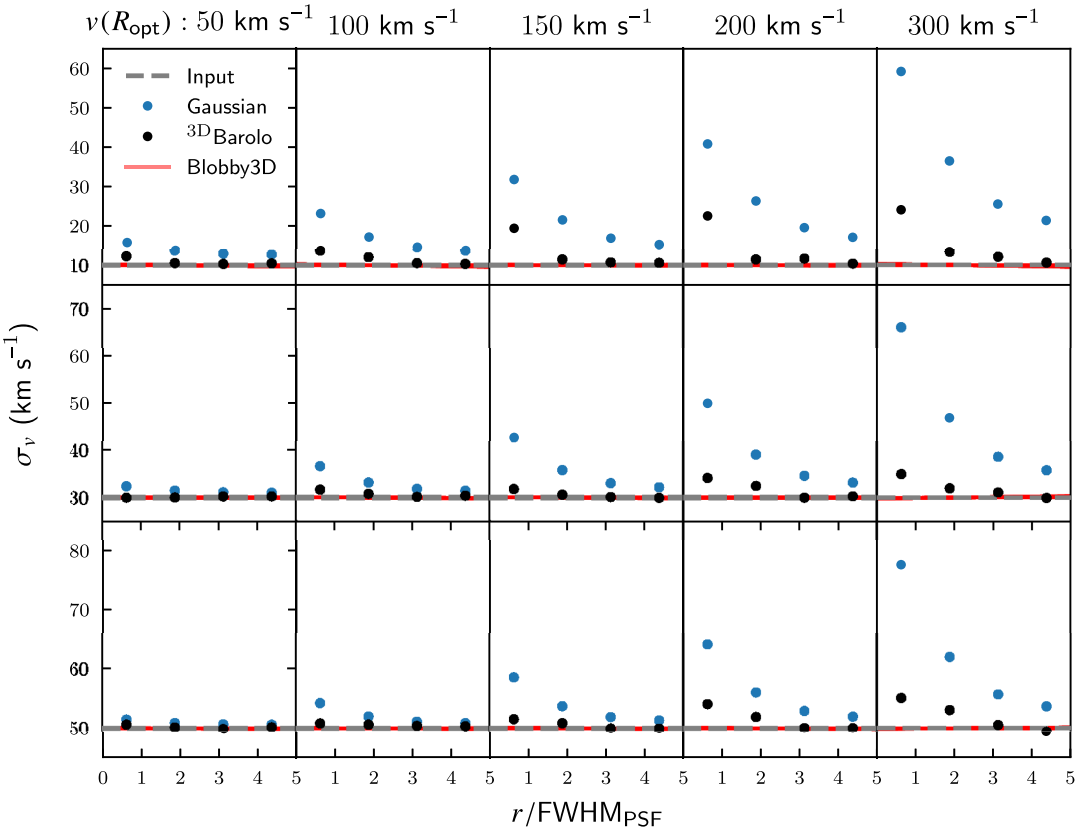

Figure 4. Recovering the LoS intrinsic radial velocity dispersion profiles for our toy models convolved by a Gaussian PSF with FWHM$_{PSF}$ = 2 arcsec. We show different $v(R_{opt})$ and $\sigma_{v,input}$ per column and row, respectively. Blue points correspond to single component Gaussian fits to each spaxel and then averaged for each radial bin. Black points correspond to the velocity dispersion estimates per ring using the ^{3D}BAROLO fitting code, and BLOBBY3D shows the posterior samples for the radial velocity dispersion profiles. We found that the relative difference between the estimated and actual LoS velocity dispersion increased towards the centre of the centre of the galaxy where the LoS velocity gradient is greatest. Similarly, these effects increased as $v(R_{opt})/\sigma_{v,input}$ increased. The estimates using ^{3D}BAROLO improve on the single-component Gaussian fit, while BLOBBY3D accurately infers the LoS velocity dispersion across the grid of toy models.

the centre of the galaxy with respect to the input velocity dispersion. This exacerbates the effect of beam smearing due to blending velocity profiles that have significantly different mean velocity compared to their width. Similarly, increasing the FWHM$_{PSF}$ acts to blend velocity gradients across wider regions of the galaxy.

We started by comparing a single component Gaussian fit to each spaxel, a tilted ring model using ^{3D}BAROLO, and our method. For the single-component Gaussian fits, we calculated the mean velocity dispersion of the spaxels across the FoV. The results for ^{3D}BAROLO were calculated using the area-weighted mean velocity dispersion across the rings. For our method, we constructed the 2D velocity dispersion map for each posterior sample and then calculated the mean velocity dispersion of the spaxels. All posterior samples are shown on this plot, but due to the negligible noise applied to the toy models the posterior distributions for the mean velocity dispersion are negligible at this scale.

To further illustrate the effect of beam smearing on the observed velocity dispersion, we show radial profiles across a grid of input $\sigma_{v,input}$ and $v(R_{opt})$ assuming a Gaussian convolution kernel with FWHM$_{PSF}$ = 2 arcsec in Fig. 4. This shows that the effect of beam smearing increases significantly in the centre of the galaxy where the velocity gradient is highest. Increasing $v(R_{opt})$ also acts to increase the velocity gradient, and thus the offsets increase as well. The effect of beam smearing decreases as the input velocity dispersion increases, suggesting that the relative relationship between $v(R_{opt})/\sigma_{v,input}$ is more indicative of the effects of beam smearing.

^{3D}BAROLO provides partial corrections for beam smearing. However, the relative difference is $\sigma_{v,out}/\sigma_{v,input} - 1 \sim 0.1$ at $v(R_{opt})$FWHM$_{PSF}/\sigma_{v,input} = 30$ arcsec and increases with $v(R_{opt})$FWHM$_{PSF}/\sigma_{v,input}$. The effect of beam smearing increases towards the centre of the galaxy as well. We suspected that the observed bias was due to ^{3D}BAROLO interpreting the unresolved velocity gradient across the discretized rings as increased velocity dispersion. Yet we found no significant difference for the estimated velocity dispersion profile when using a different number of rings. As such, the observed biases observed for ^{3D}BAROLO appear to be fundamental for low-resolution data. Di Teodoro & Fraternali (2015) also found that ^{3D}BAROLO overestimated the velocity dispersion at the centre of the galaxy for low-resolution observations (see fig. 8 in their paper).

^{3D}BAROLO is further affected when used for toy models convolved by a Moffat kernel. The divergence in the relative difference is $\sigma_{v,out}/\sigma_{v,input} - 1 \sim 0.1$ at $v(R_{opt})$FWHM$_{PSF}/\sigma_{v,input} = 10$ arcsec. In this case, we assumed the Gaussian convolution kernel used by ^{3D}BAROLO had an FWHM equal to that of the Moffat profile. As ^{3D}BAROLO assumes a Gaussian PSF, we expected that using it for a toy model convolved by a Moffat kernel would affect the estimates.

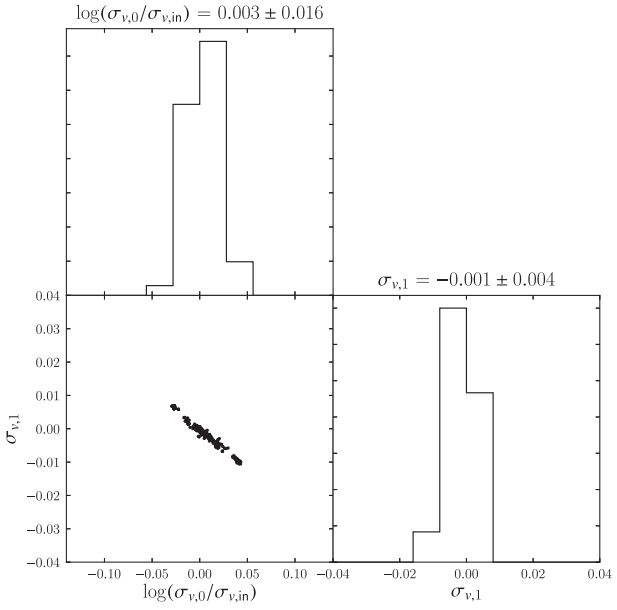

Figure 5. Marginalized posterior distributions for the log relative difference between the modelled central velocity dispersion ($\sigma_{v,0}$) and the input velocity dispersion ($\sigma_{v,\mathrm{true}}$) (top), plus the log velocity dispersion gradient ($\sigma_{v,1}$) (bottom right). We also show the conditional posterior distribution between these parameters (bottom left). We found that the distribution of our inferred intrinsic velocity dispersion parameters was consistent with our inputs.

Bouché et al. (2015) also pointed out that significant differences for the velocity dispersion estimates can be caused by not accurately modelling the PSF axial ratio. Similar issues are likely to arise when our PSF modelling assumptions are not met. We suggest that researchers keep in mind that assumptions about the PSF will affect the velocity dispersion estimates.

Our method accurately estimates the intrinsic velocity dispersion, as shown in both the relative differences in Fig. 3 and the radial profiles in Fig. 4. We also show the posterior distribution of the log relative difference $\log(\sigma_{v,0}/\sigma_{v,\mathrm{in}})$ and $\sigma_{v,1}$ in Fig. 5. These plots are marginalized over all toy models and the remaining parameters. The marginalized distributions remain consistent with zero for both parameters as $\log(\sigma_{V,0}/\sigma_{v,\mathrm{in}}) = 0.3 \pm 1.7 \times 10^{-2}$ and $\sigma_{v,1} = -1 \pm 4 \times 10^{-3}$. There is a slight tendency for higher $\sigma_{v,0}$ with negative gradients, but this was negligible as the difference in velocity dispersion compared to the input values was $<1\,\mathrm{km\,s^{-1}}$ in all cases.

3.1.2 Estimating the velocity profiles

We show the inferred velocity profiles for varying $v(R_{\mathrm{opt}})$ and $\mathrm{FWHM_{PSF}}$ in Figs 6 and 7, respectively. We only show the velocity profiles for $\sigma_{v,\mathrm{in}} = 20\,\mathrm{km\,s^{-1}}$ as we did not observe any dependence on the inferred velocity profiles as a function of the input velocity dispersion.

Once again, considering the Gaussian fits as indicative for the effects of beam smearing, we note that the velocity is typically underestimated in regions of high-velocity gradient. This relative effect on the observed velocity compared to $v(R_{\mathrm{opt}})$ is approximately constant. Instead, the differences are greatly affected by increasing the $\mathrm{FWHM_{PSF}}$. These effects are consistent with the modelling performed by Davies et al. (2011).

The effects of beam smearing remain when using ^{3D}BAROLO. We did not find any significant difference for the inferred velocity profiles when we changed the number of rings.

Our method typically estimates the velocity profile well for $v(R_{\mathrm{opt}}) \geq 150\,\mathrm{km\,s^{-1}}$. For $v(R_{\mathrm{opt}}) < 150\,\mathrm{km\,s^{-1}}$, there are issues estimating the shape of the velocity profile particular in the centre of the galaxy and the outskirts. The effects for $v(R_{\mathrm{opt}}) = 100\,\mathrm{km\,s^{-1}}$ are minimal both in relative and absolute terms. For $v(R_{\mathrm{opt}}) = 50\,\mathrm{km\,s^{-1}}$ the relative difference is $\sim$0.05 corresponding to a few $\mathrm{km\,s^{-1}}$.

The reasoning for the difference at low $v(R_{\mathrm{opt}})$ remains unclear as better 1D fits for the Courteau (1997) empirical model to the input URC are within the prior distribution. We suspect that the differences are driven by performing the full 3D modelling where the differences in model parametrization and integration are slightly different for the toy modelling compared to the BLOBBY3D approach. However, given the negligible difference compared to systematic and variance that will be involved in modelling real data, we do not consider this to be a significant issue.

3.2 A toy model with gas substructure

We then constructed a more realistic toy model. First, we constructed a toy model as defined above with $\sigma_v = 20\ \mathrm{km\ s^{-1}}$ and $v_c = 200\ \mathrm{km\ s^{-1}}$. We rotated the position angle of the disc by $\pi/4$ and added 10 Gaussian blobs to the gas distribution. All blobs were defined to be circular in the plane of the disc. The integrated flux for each blob was set to 10 per cent of the disc flux. The width for each blob was set to $w = 0.2R_e$. The centre of the blobs were randomized uniformly with distance to the centre as $r/R_e = [0, 2]$ in the plane of the disc. We distributed the polar angle uniformly in the range $\phi_c = [0, \pi]$. We add independent and identically distributed (*iid*) Gaussian noise corresponding to mean S/N = 20 per wavelength bin. The cube was oversampled then convolved as per all of our previous toy models.

The distribution of ϕ in the range $[0, \pi]$ introduces an asymmetry in the flux profile as blobs are only placed on one side of the disc. We do this to show that our method is capable of recovering asymmetric gas distributions. We also note that such substructures are common in real observations.

We show the toy model and our results in Fig. 8. An interesting consequence of introducing asymmetries in the flux profile is that convolving the model by the PSF introduces asymmetries in the velocity dispersion profile. In this case, the 2D velocity dispersion map for the convolved data shows two tails on the side where the blobs are located.

Modelling to the convolved data is performed well with no outlying structure remaining in the residual maps. Recovery of the preconvolved model is also performed reasonably well. The maximum relative difference in the map is $\sim$0.1 whereas the velocity profile is within several $\mathrm{km\ s^{-1}}$ and the maximum difference in velocity dispersion is less than 1 $\mathrm{km\ s^{-1}}$. While this posterior sample shows a very shallow positive velocity dispersion gradient ($<1\ \mathrm{km\ s^{-1}}$ difference across the FoV), there is no observed bias in the gradients in the full marginalized posterior distribution with $\sigma_{v,0} = 0.03 \pm 0.11$.

4 APPLICATIONS TO REAL DATA

We then applied the method to a sample of 20 galaxies from the SAMI Galaxy Survey. The SAMI Galaxy Survey uses SAMI (Croom et al. 2012). SAMI uses 13 fibre bundles known as

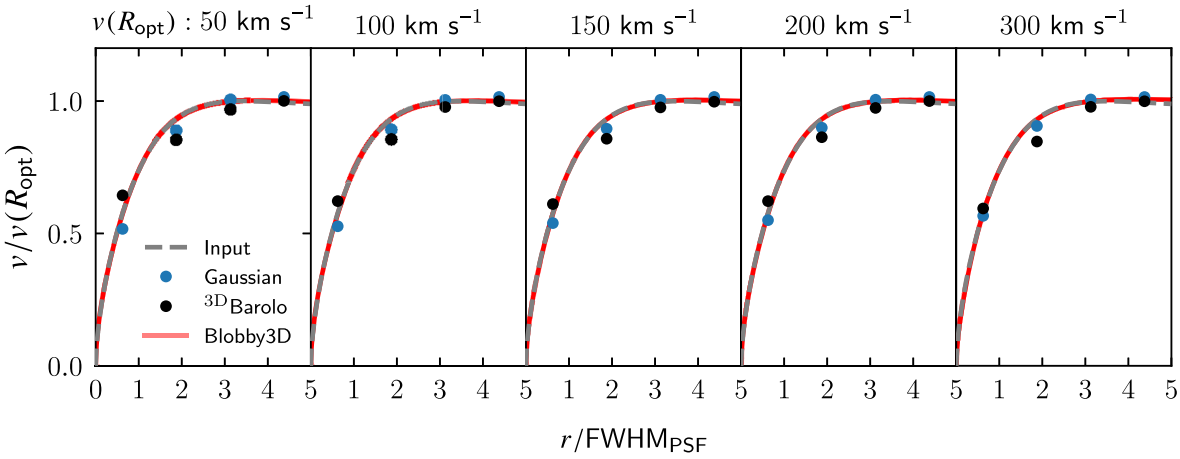

Figure 6. Recovering the velocity profile for our toy models with exponential flux distribution, URC with different $v(R_{opt})$, and $\sigma_v = 20\,km\,s^{-1}$. The toy models were convolved with a Gaussian profile with FWHM$_{PSF}$ = 2 arcsec. The toy models were constructed with negligible noise to check for systematic biases in the methodologies. Blue dots correspond to a single component Gaussian fit to each spaxel where the mean has been calculated for four equally space bins. ^{3D}BAROLO (black) shows the radial velocity in each radial bin. BLOBBY3D (red) shows 12 posterior samples for the velocity profile, although the difference for each posterior sample is negligible due to zero noise applied to the toy models. ^{3D}BAROLO does not fully recover the velocity profile at $v(R_{opt}) = 50\,km\,s^{-1}$.

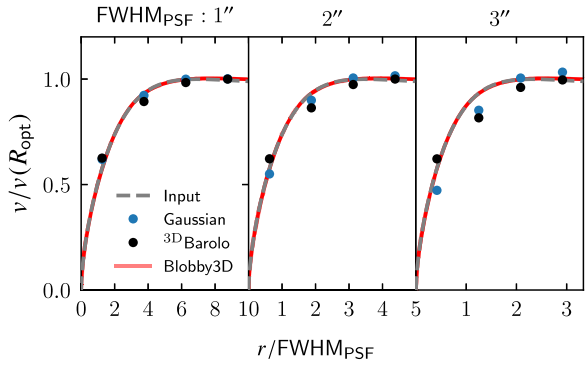

Figure 7. Similar to Fig. 6 but setting $v(R_{opt}) = 200\,km\,s^{-1}$ and varying the FWHM$_{PSF}$. In this case, we found that the inferred LoS velocity gradient is flattened for both the single component Gaussian fits to each spaxel and ^{3D}BAROLO as FWHM$_{PSF}$ increases. BLOBBY3D is not affected by increasing the FWHM$_{PSF}$.

hexabundles which consist of 61 fibres with 75 per cent filling factor that subtend 1.6 arcsec for a total FoV with width 15 arcsec (Bland-Hawthorn et al. 2011; Bryant et al. 2014). The IFUs, as well as 26 sky fibres, are plugged into pre-drilled plates using magnetic connectors. SAMI fibres are fed to the double-beam AAOmega spectrograph (Sharp et al. 2006). The SAMI Galaxy survey uses the 570V grating at 3700–5700 Å giving a resolution of $R \sim 1730$, and the R1000 grating from 6250–7350 Å giving a resolution of $R \sim 4500$.

4.1 Sample selection

The SAMI Galaxy Survey has observed >3000 galaxies. We aim to present initial results for a small sample of galaxies that are representative of typical star-forming galaxies within the parent sample. Star-forming galaxies were chosen as their gas kinematics typically have smoothly varying kinematic profiles. This is in contrast to galaxies with Hα emission associated non-star-forming mechanisms. A common example are galaxies with an active galactic nuclei (AGNs), as they typically have significantly higher velocity dispersion in the centre of the galaxy compared to the outskirts.

Star-forming galaxies were selected by applying a cut-off integrated Hα equivalent width >3 Å. The equivalent width cut-off is consistent with the star-forming main-sequence cut-off applied by Cid Fernandes et al. (2011) using single-fibre SDSS data. The equivalent width was measured as the width in the spectral dimension of a rectangle with width and height equal to a measure of the integrated continuum and Hα flux, respectively. We used the mean continuum across the wavelength range [6500 Å, 6540 Å] as the estimate for the continuum per spaxel.

We removed galaxies with Hα emission contaminated by AGNs or LINERs using the AGN classification proposed by Kauffmann et al. (2003). Under this classification, we removed galaxies under the condition that,

$$\log([\mathrm{O\,III}]/\mathrm{H}\beta) > 0.61/(\log([\mathrm{N\,II}]/\mathrm{H}\alpha) - 0.05) + 1.3, \quad (25)$$

where [O III] and [N II] represent the emission lines at 5007 and 6583 Å, respectively. For each emission line, we used the integrated flux estimates in the 1.4 arcsec aperture spectra data provided in the SAMI Galaxy Survey DR2 (Scott et al. 2018). The 1.4 arcsec aperture spectra data are the innermost aperture spectra data provided in SAMI Galaxy Survey DR2, and thus should be the most appropriate to find galaxies with AGN or LINER emission which is typically centrally concentrated.

We selected galaxies with an intermediate inclination angle ($i \in [30°, 60°]$). Galaxies with low inclination were avoided as it is difficult to infer the velocity profile. Whereas galaxies close to edge-on will be difficult to model as our method assumes a thin disc. Furthermore, galaxies observed close to edge-on are typically optically thick, such that the entire disc cannot be observed. The inclination estimates were calculated by converting an estimate for the observed ellipticity assuming a thin disc. Similarly, we selected galaxies with intermediate effective radius ($R_e \in [2.5$ arcsec, 22.5 arcsec]). This avoids small galaxies that are not well resolved. It also ignores large galaxies which may be difficult to infer their velocity profile. Estimates for the ellipticity and effective radius

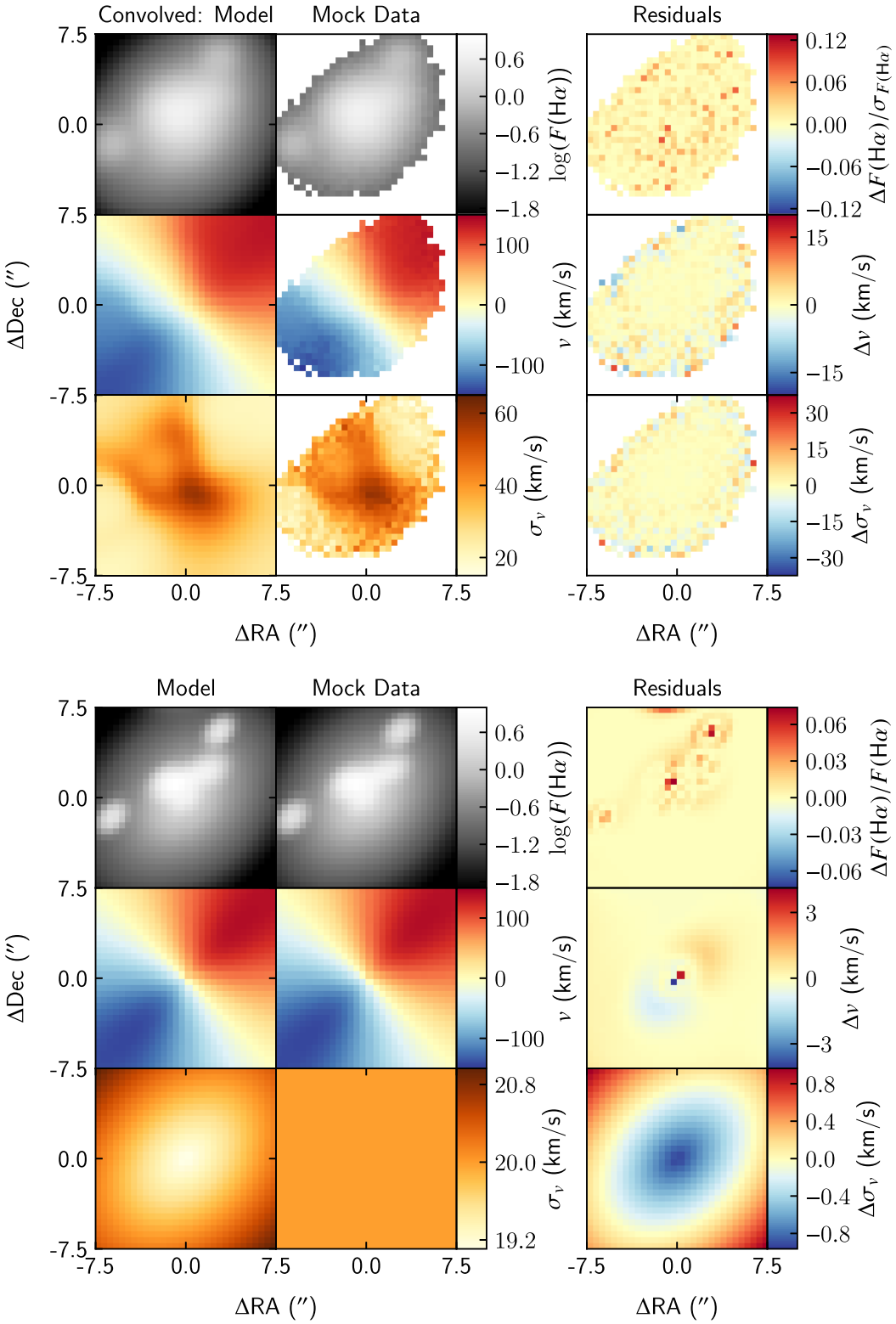

Figure 8. 2D maps for a posterior sample for a toy model with asymmetric gas substructure. For the top three rows, we show the convolved model compared to the convolved mock data (i.e. toy model). The preconvolved BLOBBY3D model and preconvolved mock data are compared in the bottom three rows. In both cases the rows show the Hα flux, LoS velocity profile, and LoS velocity dispersion. The columns show the respective BLOBBY3D output, data, and residuals. The absolute residuals are shown for the velocity and velocity dispersion maps. In the top panel we show the flux map residuals normalized with respect to the modelled Gaussian noise, whereas in the bottom panel we show the relative flux difference. The convolved mock data are shown where Hα flux S/N > 10. We found that convolving a model with gas substructure and radial kinematic profiles introduced kinematic asymmetries. BLOBBY3D was able to model the gas and kinematic profile asymmetries and recover the intrinsic gas kinematics accurately.

Table 2. Summary statistics for our sample of galaxies from the SAMI galaxy survey. All values are sourced from the SAMI parent catalogue described by Bryant et al. (2015). We also show the estimated SAMI Galaxy Survey pipeline estimated values for the PSF assuming a Moffat profile.

GAMA ID	RA (°)	Dec. (°)	z_{spec}	$\log(M_*/M_\odot)$	R_e (arcsec)	e	$FWHM_{PSF}$ (arcsec)	β_{PSF}
214245	129.524 46	0.608 96	0.014	9.40	4.46	0.32	2.12	3.65
220371	181.23715	1.508 24	0.020	9.53	6.97	0.35	3.37	6.78
220578	182.178 17	1.456 36	0.019	8.98	2.96	0.41	2.34	2.71
238395	214.243 19	1.640 43	0.025	9.87	4.11	0.18	3.29	4.76
273951	185.930 37	1.311 09	0.026	8.72	4.34	0.45	1.62	2.77
278804	133.859 39	0.858 18	0.042	9.82	2.65	0.38	2.87	4.03
298114	218.400 91	1.305 90	0.056	10.25	4.84	0.41	2.26	4.01
30346	174.638 65	− 1.184 49	0.021	10.45	11.25	0.32	1.89	2.48
30377	174.822 86	− 1.079 31	0.027	8.22	3.81	0.35	3.30	3.81
30890	177.257 96	− 1.102 60	0.020	9.79	7.56	0.43	2.92	3.94
422366	130.595 60	2.497 33	0.029	9.62	8.86	0.49	1.78	2.49
485885	217.757 90	− 1.717 21	0.055	10.25	5.04	0.16	2.27	5.19
517167	131.161 37	2.410 98	0.030	9.24	3.67	0.31	2.01	2.81
55367	181.793 34	− 0.259 59	0.022	8.40	6.71	0.30	1.56	3.64
56183	184.852 45	− 0.294 10	0.039	9.50	3.58	0.23	2.18	3.19
592999	215.061 56	− 0.079 38	0.053	10.26	4.24	0.47	1.53	2.98
617655	212.635 06	0.224 18	0.029	9.07	5.08	0.14	2.85	8.67
69620	175.724 73	0.161 89	0.018	9.30	4.45	0.25	2.53	4.49
84107	175.998 43	0.428 01	0.029	9.71	5.05	0.23	2.53	4.49
85423	182.278 32	0.473 28	0.020	8.63	3.56	0.18	2.90	3.55

were taken from the SAMI Galaxy Survey parent catalogue (Bryant et al. 2015), who in turn used the single Sérsic fits to the *r*-band Sloan Digital Sky Survey images by Kelvin et al. (2012).

There are 330 galaxies that meet the above criteria in the SAMI Galaxy Survey DR2. We chose 20 galaxies with our final galaxy sample shown in Table 2.

4.2 Data cubes

The data cubes we used were from the SAMI internal data release v0.10.1 (Scott et al. 2018). Data cubes were redshift corrected by the spectroscopic redshift which was taken from the SAMI parent catalogue (Bryant et al. 2015) who used the estimates from the Galaxy and Mass Assembly (GAMA) survey (Driver et al. 2011).

The data cubes were then cut around the Hα emission line by $\pm 500\,\mathrm{km\,s^{-1}}$. In our sample, this was wide enough to observe the full Hα emission line while avoiding significant influence from the adjacent [N II] emission lines.

The continuum model used to subtract from the data cubes were the single-component LZIFU (Ho et al. 2016) data products from the SAMI Galaxy Survey internal data release v0.10.1. LZIFU uses the penalized pixel-fitting routine (PPXF; Cappellari & Emsellem 2004) to model the continuum using a combination of spectral stellar population templates.

Poor continuum modelling can cause systematics in the data cube that are not well represented in the galaxy model parametrization. While we could extend the systematic parametrization to account for systematics introduced by poor continuum modelling, such corrections would likely require a large number of nuisance parameters that would be difficult to marginalize over. Instead, we masked pixels with Hα flux signal-to-noise <3 and performed a secondary fit to the data using a Gaussian plus linear continuum estimate to the region cut around the Hα line. The continuum estimated from this fit was then subtracted from the data.

4.3 Results

For completeness, we show our estimates of the marginalized distributions for all parameters, omitting individual blob parameters, in Tables 3 and 4. We also show 2D maps of an example posterior sample for GAMA 485885 and 220371 in Fig. 9. A galaxy with asymmetric substructure observed in the gas kinematics is shown in 10. These example posterior samples show the ability of our method to fit complex substructure. Note that the exact shape of each blob does change per posterior sample, so these should only be considered for illustrative purposes.

For GAMA 485885, we see the ability of our approach to resolve a classic spiral gas distribution. The 2D residuals between the convolved model and data exhibit significant differences on scales less than the $FWHM_{PSF}$. The 2D maps for the LoS gas kinematics suggest that the gas is approximately regularly rotating around a kinematic centre, potentially with a small warp in the kinematic position angle. The Hα gas velocity dispersion is peaked within the centre of the galaxy as expected for most regularly rotating galaxies that have been affected by beam smearing.

We show 2D maps for GAMA 220371 in Fig. 9. This galaxy has a clumpy Hα gas profile. We are still able to construct an adequate model to the data using our approach. The 2D residual maps for the Hα flux show greater differences for three clumps in the north-east, south-east, and south-west regions. However, the general structure of the clumps is reasonably well resolved. The maps for the gas kinematics suggest an approximately regularly rotating galaxy. The velocity dispersion map does not show a significant peak in the centre of the galaxy compared to GAMA 485885. This is likely driven by having a shallower LoS velocity gradient and less centralized Hα gas flux compared to GAMA 485885.

An example posterior sample for GAMA 30890 is shown in Fig. 10. This galaxy exhibits asymmetries and substructure in the LoS Hα gas kinematic maps. We are able to partially recover the Hα

Table 3. Inferences for global parameters and blob hyperparameters for our sample of galaxies from the SAMI Galaxy Survey. We show the mean and standard deviation for the marginalized distribution for each parameter. Note that flux units are 10^{-16} erg s^{-1} cm^{-2}.

GAMA ID	N	PA (°)	μ_r (arcsec)	μ_F	σ_F	$W_{\rm max}$ (arcsec)	$q_{\rm min}$	$\log(\sigma_0)$
214245	79 ± 17	304.4 ± 0.2	24 ± 5	2.5 ± 0.6	1.2 ± 0.3	1.05 ± 0.07	0.206 ± 0.007	− 3.43 ± 0.04
220371	117 ± 20	332.05 ± 0.09	25 ± 4	4.2 ± 1.0	1.3 ± 0.2	1.81 ± 0.06	0.25 ± 0.02	− 3.09 ± 0.01
220578	20 ± 7	22.2 ± 0.1	13 ± 7	46 ± 7	0.4 ± 0.2	0.504 ± 0.004	0.29 ± 0.04	− 2.445 ± 0.004
238395	173 ± 45	163.11 ± 0.07	21 ± 6	20 ± 11	1.9 ± 0.4	0.5009 ± 0.0008	0.36 ± 0.02	− 1.569 ± 0.002
273951	15 ± 4	30.2 ± 0.7	5 ± 3	28 ± 14	1.8 ± 0.4	0.5005 ± 0.0005	0.22 ± 0.02	− 1.508 ± 0.003
278804	18 ± 3	209 ± 1	1.9 ± 0.7	4 ± 1	1.0 ± 0.2	0.51 ± 0.02	0.28 ± 0.07	− 2.073 67 ± 0.00003
298114	112 ± 25	272.80 ± 0.03	21 ± 6	15.4 ± 0.7	0.32 ± 0.05	1.92 ± 0.04	0.203 ± 0.004	− 2.461 ± 0.005
30346	70 ± 9	304.32 ± 0.02	26 ± 5	72 ± 5	0.46 ± 0.08	2.31 ± 0.04	0.23 ± 0.01	− 2.009 ± 0.003
30377	79 ± 23	173 ± 1	21 ± 6	1.1 ± 0.4	1.0 ± 0.3	0.51 ± 0.01	0.7 ± 0.2	− 8 ± 2
30890	100 ± 17	19.35 ± 0.03	22 ± 5	23 ± 2	0.71 ± 0.08	2.31 ± 0.05	0.24 ± 0.01	− 2.587 ± 0.003
422366	159 ± 29	258.37 ± 0.10	26 ± 3	5 ± 1	0.9 ± 0.2	0.6 ± 0.1	0.23 ± 0.03	− 2.2229 ± 0.0002
485885	130 ± 33	353.0 ± 0.1	19 ± 6	2.8 ± 0.4	0.79 ± 0.09	0.5007 ± 0.0008	0.202 ± 0.002	− 3.38 ± 0.03
517167	59 ± 16	359.58 ± 0.10	21 ± 6	7 ± 3	1.5 ± 0.3	1.2 ± 0.1	0.203 ± 0.004	− 2.634 ± 0.004
55367	177 ± 46	182.8 ± 0.1	24 ± 4	0.5 ± 0.2	1.5 ± 0.2	0.79 ± 0.04	0.202 ± 0.002	− 8 ± 2
56183	115 ± 34	264.27 ± 0.07	15 ± 7	1.9 ± 0.7	1.9 ± 0.3	1.18 ± 0.03	0.42 ± 0.03	− 2.760 ± 0.004
592999	98 ± 22	223.90 ± 0.05	20 ± 6	7 ± 1	1.0 ± 0.1	2.24 ± 0.05	0.207 ± 0.005	− 2.362 ± 0.003
617655	117 ± 26	316.5 ± 0.1	23 ± 5	1.9 ± 0.4	1.0 ± 0.1	1.29 ± 0.04	0.42 ± 0.02	− 8 ± 2
69620	152 ± 25	300.20 ± 0.07	23 ± 4	17 ± 2	0.65 ± 0.06	0.5002 ± 0.0002	0.28 ± 0.03	− 2.072 ± 0.002
84107	110 ± 23	274.66 ± 0.04	23 ± 5	19 ± 4	1.2 ± 0.2	0.5001 ± 0.0001	0.544 ± 0.010	− 1.775 ± 0.002
85423	87 ± 24	251.2 ± 0.3	23 ± 5	1.1 ± 0.7	1.6 ± 0.4	1.09 ± 0.05	0.48 ± 0.06	− 8 ± 2

Table 4. Inferences for galaxy kinematic parameters for our sample of galaxies from the SAMI Galaxy Survey. We show the mean and standard deviation for the marginalized distribution for each parameter.

GAMA ID	$v_{\rm sys}$ (km s^{-1})	v_c (km s^{-1})	r_t (arcsec)	γ_v	β_v	$\sigma_{v,0}$ (km s^{-1})	$\sigma_{v,1}$
214245	− 11.5 ± 0.1	71 ± 1	3.69 ± 0.04	81 ± 12	− 0.36 ± 0.03	25.7 ± 0.6	− 0.087 ± 0.005
220371	− 5.03 ± 0.08	178 ± 5	8.0 ± 0.3	1.43 ± 0.08	− 0.24 ± 0.03	23.0 ± 0.5	− 0.031 ± 0.003
220578	− 15.6 ± 0.3	72 ± 1	6.2 ± 0.1	58 ± 22	0.71 ± 0.01	20.6 ± 0.5	− 0.104 ± 0.009
238395	− 3.58 ± 0.08	147 ± 3	2.5 ± 0.4	1.03 ± 0.03	0.31 ± 0.05	27.3 ± 0.2	0.023 ± 0.002
273951	5.95 ± 0.08	242 ± 81	15 ± 3	17 ± 24	− 0.71 ± 0.04	33.0 ± 0.9	− 0.17 ± 0.03
278804	− 16.4 ± 0.8	140 ± 2	6.5 ± 0.2	3.8 ± 0.5	0.662 ± 0.008	26 ± 2	− 0.21 ± 0.05
298114	5.19 ± 0.07	180.6 ± 0.4	2.051 ± 0.009	93 ± 8	− 0.149 ± 0.006	21.4 ± 0.3	0.001 ± 0.002
30346	2.09 ± 0.08	183.7 ± 0.2	0.684 ± 0.009	94 ± 6	− 0.08 ± 0.02	12.3 ± 0.3	0.051 ± 0.003
30377	5.4 ± 0.3	274 ± 55	13 ± 2	21 ± 24	− 0.70 ± 0.04	18.1 ± 0.5	0.023 ± 0.006
30890	− 7.64 ± 0.05	134.0 ± 0.4	1.20 ± 0.07	1.24 ± 0.02	− 0.47 ± 0.06	23.7 ± 0.1	0.001 ± 0.001
422366	− 12.8 ± 0.3	78 ± 1	5.53 ± 0.07	17 ± 8	0.52 ± 0.02	18.3 ± 0.4	0.018 ± 0.003
485885	− 5.6 ± 0.1	129 ± 6	4.3 ± 0.1	2.8 ± 0.4	0.67 ± 0.03	21.8 ± 0.3	− 0.017 ± 0.003
517167	− 9.80 ± 0.10	73.5 ± 0.5	4.38 ± 0.02	92 ± 8	0.593 ± 0.009	13.8 ± 0.2	0.075 ± 0.004
55367	− 10.2 ± 0.1	70 ± 5	27 ± 2	32 ± 26	0.40 ± 0.02	14.9 ± 0.7	− 0.15 ± 0.01
56183	− 6.99 ± 0.09	111 ± 2	4.8 ± 0.3	1.21 ± 0.03	0.58 ± 0.01	31.6 ± 0.2	− 0.076 ± 0.002
592999	− 17.00 ± 0.10	185 ± 3	7.5 ± 0.1	1.85 ± 0.06	0.601 ± 0.009	33.8 ± 0.5	− 0.061 ± 0.003
617655	8.07 ± 0.09	86 ± 3	3.9 ± 0.1	10 ± 3	0.26 ± 0.06	14.0 ± 0.4	0.039 ± 0.006
69620	3.86 ± 0.08	106 ± 3	19.5 ± 0.9	2.7 ± 0.2	0.590 ± 0.008	20.6 ± 0.1	0.021 ± 0.001
84107	7.25 ± 0.06	99.5 ± 0.6	3.62 ± 0.01	96 ± 4	0.34 ± 0.01	25.1 ± 0.3	0.017 ± 0.003
85423	94 ± 2	177 ± 5	5.33 ± 0.09	32 ± 22	− 0.68 ± 0.03	19 ± 1	− 0.07 ± 0.02

gas kinematics despite only introducing asymmetries in the gas Hα gas distribution. Some substructure in the residuals remain with a patch of Hα gas flux that is lower in the convolved model compared to data. There is also a slight warp in the LoS velocity profile as a function of radius, and differences in the velocity dispersion of the order of 5 km s^{-1}. However, the convolved model still performs reasonably well at resolving the gas flux and kinematics. Our ability to partially resolve the gas kinematic asymmetries suggests that the Hα gas distribution plus beam smearing can result in gas substructures that are not necessarily present in the underlying data. This is similar to the results we saw in Fig. 8, where we showed that introducing asymmetric substructure in the gas distribution for a regularly rotating toy model plus beam smearing led to substructure in the gas kinematics.

The SAMI Galaxy Survey provides gas kinematic data products estimated using the LZIFU package (Ho et al. 2016). LZIFU performs single and multiple Gaussian component fits to the emission lines. Corrections for instrumental broadening are performed by subtracting the LSF from the velocity dispersion in quadrature. Effects of beam smearing are not considered.

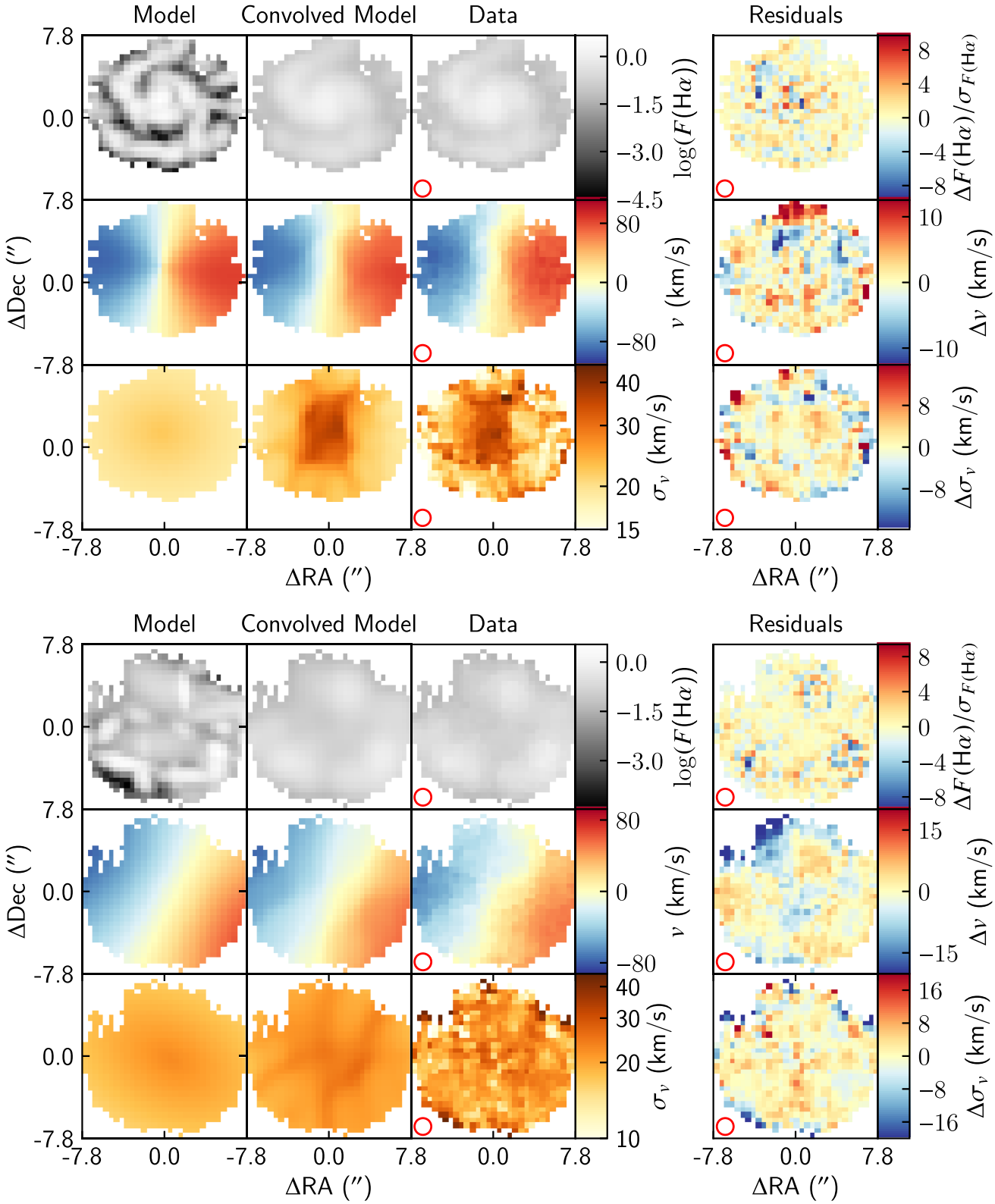

Figure 9. 2D maps for a single posterior sample for GAMA 485885 (top) and 220371 (bottom). For each galaxy we show from left to right the model, convolved model, single-component Gaussian fits to the data, and 2D residuals where $\Delta F(\mathrm{H}\,\alpha) = F(\mathrm{H}\,\alpha, \mathrm{ConvolvedModel}) - F(\mathrm{H}\,\alpha, \mathrm{Data})$. The flux map residuals have been normalized with respect to the modelled Gaussian noise, whereas the absolute difference is shown for the velocity and velocity dispersion maps. Red circles with $r = \mathrm{FWHM_{PSF}}$ indicate the seeing width. The rows show the H α flux, LoS velocity profile, and LoS velocity dispersion. Spaxels are shown where the data H α flux S/N > 10. These examples show the ability of BLOBBY3D to model galaxies with spirals and clumpy profiles. Parametrizing complex gas distributions such as observed in the these galaxies is typically difficult, but they are a natural output of our approach.

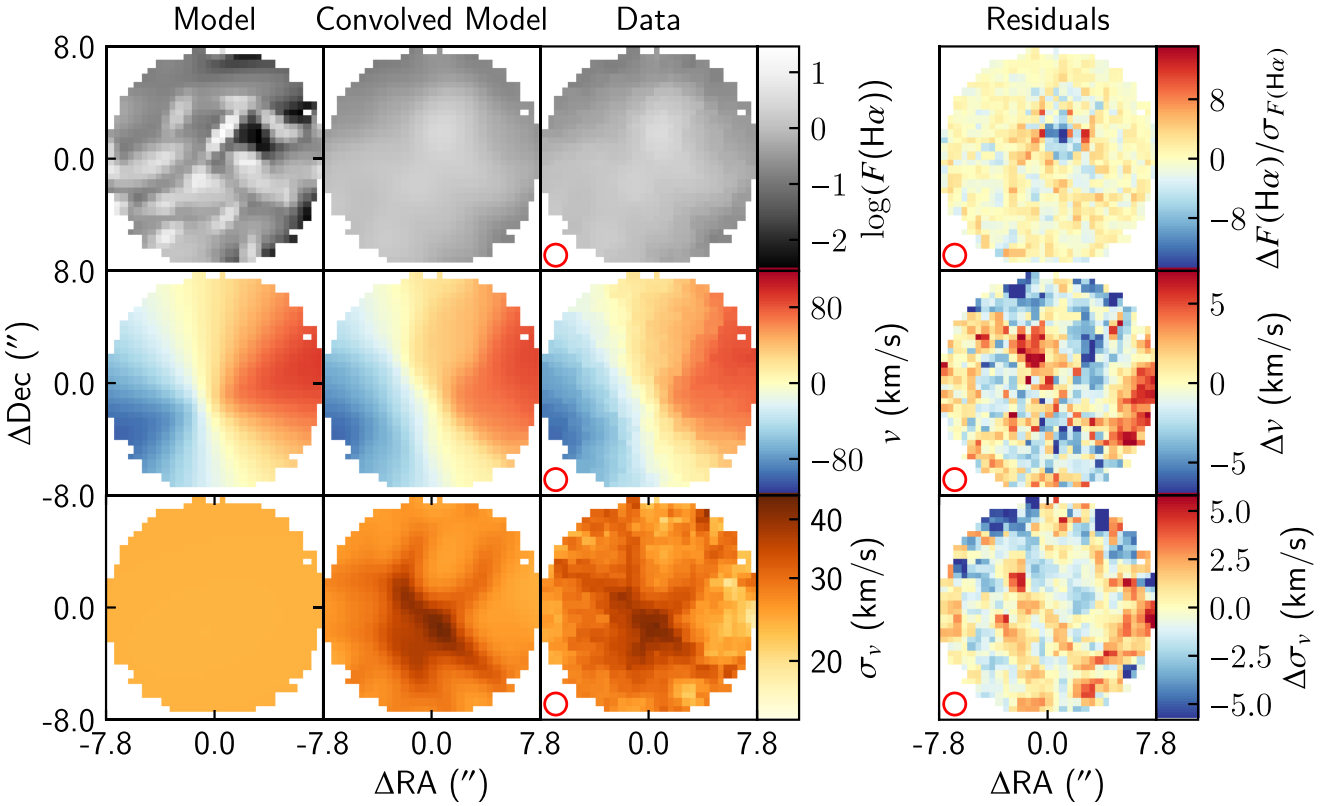

Figure 10. Same as Fig. 9 for GAMA 30890. This galaxy exhibits asymmetric substructure in the Hα gas kinematic maps. BLOBBY3D partially recovers the kinematic asymmetries despite only introducing asymmetric substructure in the Hα gas distribution. This is similar to the asymmetries modelled for our toy model with gas substructure in Fig. 8. This suggests that beam smearing can play a role in the observed substructure for the Hα gas kinematics.

A comparison between inferences for the global velocity dispersion between the single component LZIFU data products and our method are shown in Fig. 11. We compare the uniformly weighted ($\bar{\sigma}_v$) and Hα flux-weighted ($\bar{\sigma}_{v,\mathrm{H}\alpha}$) mean velocity dispersion across the FoV. We only consider spaxels with Hα signal-to-noise > 10 as estimated by LZIFU. This was primarily due to the increased scatter in the LZIFU estimates for the Hα gas velocity dispersion in the low signal-to-noise regions.

Estimates of the global velocity dispersion using our method are in the range $\sim$[7, 30] km s^{-1} using both the unweighted and Hα flux-weighted mean. This is in comparison to estimates using the single-component LZIFU data products of $\sim$[10, 45] km s^{-1}.

The mean relative corrections per galaxy ($\Delta\bar{\sigma}_v/\bar{\sigma}_V$) from our method is -0.33 ± 0.19 and -0.29 ± 0.18 when comparing $\bar{\sigma}_v$ and $\bar{\sigma}_{v,\mathrm{H}\alpha}$, respectively. Absolute corrections for the Hα flux-weighted mean velocity dispersion were -9^{+7}_{-13} km s^{-1}.

In Fig. 11, the data are colour-coded by FWHM$_{\mathrm{PSF}}$ (left) and v_c (right). Qualitatively, we do not find significant trends for our corrections as a function of either of these parameters. We did expect to see a relationship between these parameters and our velocity dispersion corrections as that would be consistent with our toy model results. A larger sample of galaxies is probably required to find clear relationships between these variables and our corrections.

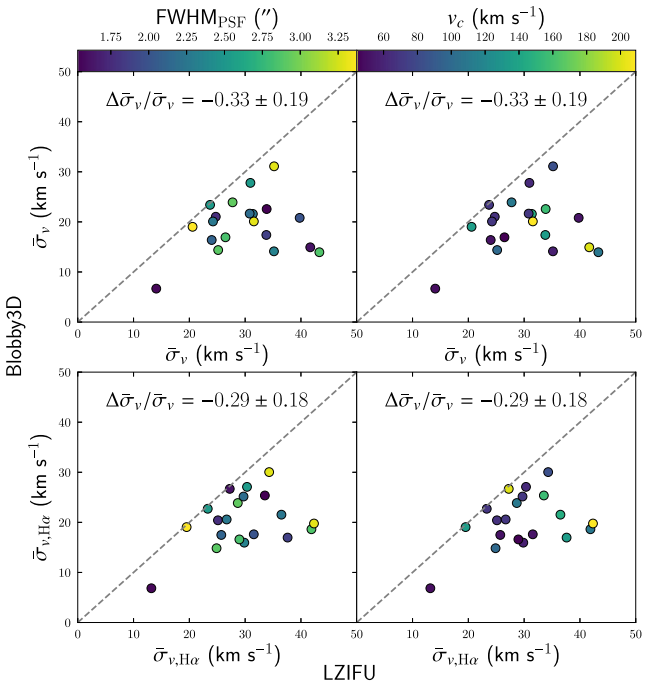

Figure 11. Comparing estimates for the mean velocity dispersion using maps from the LZIFU data products and 2D maps of our method. The comparisons calculated for the unweighted (top) and Hα flux-weighted (bottom) mean of the 2D velocity dispersion maps. $\Delta\bar{\sigma}_v/\bar{\sigma}_v$ is the arithmetic mean relative correction. We found that BLOBBY3D made significant corrections to the velocity dispersion estimates inferred by LZIFU.

5 DISCUSSION

5.1 Estimating global velocity dispersion

Beam smearing is well-known to researchers that study spatially resolved spectroscopy. As such, there have been a number of

approaches to correct for beam smearing in the literature. Most of this focus has been on correcting for the global velocity dispersion.

5.1.1 *Heuristic approaches*

A number of heuristic calculational approaches have been developed in an effort to estimate the intrinsic global velocity dispersion. A popular approach is to calculate an estimator of the velocity dispersion in regions away from the centre of the galaxy where beam smearing is expected to be negligible (e.g. Johnson et al. 2018).

Another approach is to perform corrections for a global velocity dispersion estimator as a function of factors that drive beam smearing. For example, Johnson et al. (2018) derived corrections for the median velocity dispersion and the velocity dispersion in the outskirts of the galaxy as a function of the rotational velocity and the PSF width compared to the disc width. The functional form was estimated using a grid of toy models. Using this method, they estimated relative corrections for the median velocity dispersion as $\Delta\bar{\sigma}_v/\bar{\sigma}_v = 0.2^{+0.3}_{-0.1}$ for a sample of star-forming galaxies at $z \sim 1$ using data from the KMOS Redshift One Spectroscopic Survey (KROSS). Their relative corrections for the velocity dispersion are similar to those found in this paper. However, the median seeing for KROSS was 0.7 arcsec corresponding to 5.4 kpc at the median redshift of their sample. In comparison, the mean seeing for the SAMI Galaxy Survey is 2.06 arcsec (Scott et al. 2018), corresponding to 1.75 kpc at the mean redshift of $z = 0.043$ of the full SAMI Galaxy Survey sample. As such, the effect due to beam smearing on the observed velocity dispersion are expected to be greater for KROSS.

Johnson et al. (2018) also studied a sample of star-forming galaxies from the SAMI Galaxy Survey. They estimated global velocity dispersions for individual galaxies in the range $\sigma_v \sim [20, 60]$ km s^{-1} with one galaxy scattering as high as $\sim$90 km s^{-1}. Global velocity dispersions as high as 60 km s^{-1} may suggest that they have not fully accounted for beam smearing across all of the galaxies within their sample of galaxies from the SAMI Galaxy Survey. However, given that we have only studied a small sample of galaxies from the SAMI Galaxy Survey, we cannot definitively rule out such high global velocity dispersions.

Another approach to correct for the effects of beam smearing on the observed velocity dispersion is to perform corrections based on the local velocity gradient ($v_{\rm grad}$). Varidel et al. (2016) proposed calculating the local velocity gradient using a finite-difference scheme and then performed a regression analysis to estimate the observed velocity dispersion when the local velocity gradient is zero. Zhou et al. (2017) and Federrath et al. (2017b) have also used the finite-difference scheme method to remove spaxels where the velocity gradient is much greater than the observed velocity dispersion. We note that Zhou et al. (2017) used this approach to estimate the global Hα gas velocity dispersion in the range $\sigma_v \sim [20, 30]$ km s^{-1} with an outlier (GAMA 508421) estimated to be $\sigma_v = 87 \pm 44$ km s^{-1}. We note that GAMA 508421 has observed velocity dispersion of $\sim$100 km s^{-1} in the galaxy centre that that has not been removed. It's possible that this peak is associated with beam smearing. Similarly, Oliva-Altamirano et al. (2018) subtract the local velocity gradient from the observed velocity dispersion in quadrature.

We reproduce these methods on our toy models. First, we revisit the finite-difference scheme and note that the magnitude of the local 1D gradient for a non-boundary spaxel is,

$$\left|\frac{\partial v}{\partial y}\right|_{y_i} \approx \left|\frac{v_{i+1} - v_{i-1}}{2\Delta y}\right|, \tag{26}$$

where i is the index and Δy is the width of the spaxel in the y-direction. The boundary pixels are estimated using the boundary pixel and the adjacent pixel. For a left-sided boundary, the estimated velocity gradient is then,

$$\left|\frac{\partial v}{\partial y}\right|_{y_0} \approx \left|\frac{v_1 - v_0}{\Delta y}\right|. \tag{27}$$

The total absolute magnitude of the velocity gradient is calculated by adding the orthogonal gradients in quadrature,

$$v_{\rm grad}(i, j) = \sqrt{\left|\frac{\partial v}{\partial x}\right|^2_{(i,j)} + \left|\frac{\partial v}{\partial y}\right|^2_{(i,j)}}. \tag{28}$$

This expands the previous method to include estimates for the boundary pixels. We also note that within the central pixels the division by $2\Delta y$ was omitted previously by Varidel et al. (2016). Strictly speaking, this is incorrect as the gradient will be overestimated by a factor of 2. Note that the velocity gradient is in units km s^{-1} arcsec^{-1}. To make appropriate comparisons between σ_v and $v_{\rm grad}$, we must convert these to the same units. The most natural scale parameter is the width of the PSF, we choose the FWHM$_{\rm PSF}$ and multiply it by $v_{\rm grad}$.

We then repeat the analyses performed previously with the above alterations. We show our results in Fig. 12, including comparison to a single-component Gaussian model per spaxel and our methodology. These methods provide significant corrections from the naive single-component Gaussian fits. However, our method still outperforms these methodologies across our set of toy models.

Overestimates in regions where beam smearing is high occur for estimates of the mean velocity dispersion where $\sigma_v \gg v_{\rm grad}$FWHM$_{\rm PSF}$. Increasing the cut-off did not result in significantly different estimates of the mean velocity dispersion. Overestimation is unsurprising as the effect of beam smearing on the observed velocity dispersion occur for several factors of the FWHM$_{\rm PSF}$ where the observed velocity gradient is negligible as seen in Fig. 4.

For the parametric regression estimates we fit a cubic to σ_v versus $v_{\rm grad}$ and then estimated the line at $v_{\rm grad} = 0$ km s^{-1} arcsec^{-1}. We fit a cubic instead of a first-order line in contrast to Varidel et al. (2016) as there were clear residuals observed by-eye in the linear and quadratic fits to the data. This method suffered from overestimates of the mean velocity dispersion similar to that observed using the estimates in regions where $\sigma_v \gg v_{\rm grad}$FWHM$_{\rm PSF}$. We suspect this is driven by the observed velocity gradient being shallower than the underlying velocity gradient.

The in quadrature estimates underestimate the mean velocity dispersions for $5 \lesssim v(R_{\rm opt})$FWHM$_{\rm PSF} \lesssim 30$. Adjusting a correction parameter α such that the corrections were of the form $\sqrt{\sigma_v^2 - \alpha(v_{\rm grad}{\rm FWHM}_{\rm PSF})^2}$ did not yield significant improvement. We note that Oliva-Altamirano et al. (2018) estimated the local velocity gradient after using GBKFIT to estimate the underlying velocity gradient. As such, their estimate for the velocity profile should be less affected by beam smearing, and their velocity gradient will be smooth following a parametric radial profile. They also focused on differences from the mean velocity dispersion, which may not be effected by the precision of the estimate for the global velocity dispersion.

We also note that this is an idealized toy model with negligible noise. In practice, the noise will increase the uncertainties on the

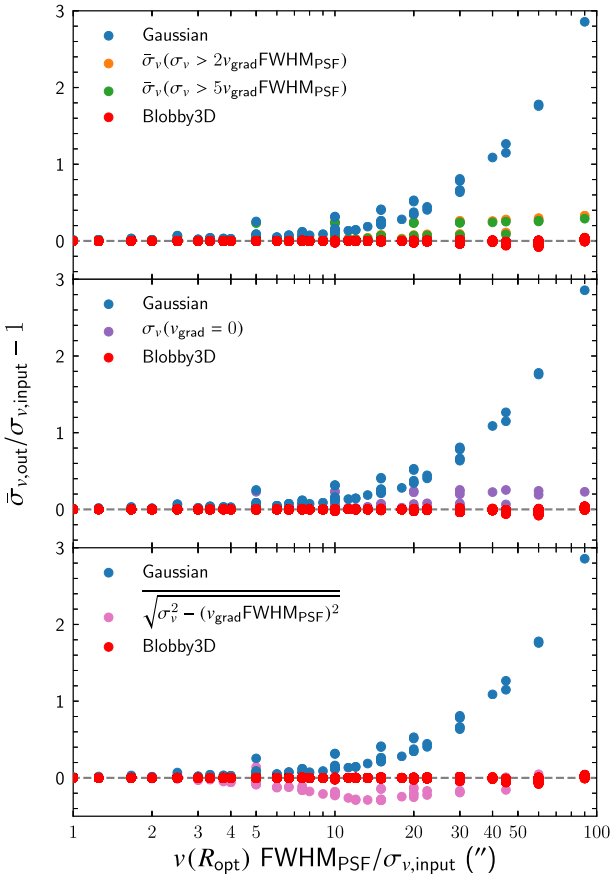

Figure 12. Using heuristic approaches to estimating the mean velocity dispersion for the toy models convolved by a Gaussian PSF using corrections from the observed local velocity gradient ($v_{\rm grad}$). Top: estimates in regions where the velocity dispersion is greater than a cutoff value of ${\rm FWHM_{PSF}}v_{\rm grad}(i, j)$. Middle: estimates the velocity dispersion at $v_{\rm grad} = 0$ by fitting a cubic to σ_v versus $v_{\rm grad}$. Bottom: in quadrature subtraction of $v_{\rm grad}$ from the observed velocity dispersion. In all cases, these approaches provide significant corrections for the intrinsic mean velocity dispersion compared to the single component Gaussian fits. However, the results from BLOBBY3D provide the most robust estimates for the intrinsic velocity dispersion.

local velocity dispersion, which will cause significant deviations in the estimates of the mean velocity dispersion. This could be improved by fitting a velocity profile across the galaxy and using the local velocity gradient derived from that profile similar to Oliva-Altamirano et al. (2018).

Furthermore, we only applied the velocity gradient approaches to toy models with no gas substructure. As we showed in Figs 8 and 10, beam smearing complex gas substructure can have significant effects on the observed gas kinematics. This will effect the estimates for the $v_{\rm grad}$, and thus will affect the ability to estimate the underlying velocity dispersion.

These heuristic approaches still provide corrections to the observed velocity dispersion. They are also easy to implement as they use a small number of related parameters (e.g. velocity gradient, width of the PSF, and distance from the centre of the galaxy). As such, they may be appropriate for particular research purposes.

As with any heuristic approaches, they often suffer from their simplicity in application. In this case, these methods cannot simultaneously model the beam smearing effect as it acts on the underlying gas and kinematic profiles. They also suffer from not fully taking into account the shape-parameters of the PSF, instead using a single measure of the PSF width such as the FWHM. 3D cube fitting algorithms are the only known approach to the authors that can perform such self-consistent modelling.

5.1.2 3D cube fitting algorithms

There are several 3D cube fitting approaches that have been proposed in the literature. Three of those are publicly available and are specifically designed to work for optical observations. Those are GALPAK3D (Bouché et al. 2015), GBKFIT (Bekiaris et al. 2016), and ^{3D}BAROLO (Di Teodoro & Fraternali 2015).

As seen in Section 3, ^{3D}BAROLO has issues resolving the kinematic profiles in low-resolution observations. This leads to overestimated velocity dispersion and shallower velocity gradients. Our testing showed no significant difference in the inferred kinematics when running ^{3D}BAROLO with a differing number of rings.

We have no reason to believe that GALPAK3D or GBKFIT suffer from similar problems. Limitations of GALPAK3D and GBKFIT are due to the inflexibility of the model parametrization which will lead to significant residuals for galaxies where complex substructure can be observed. The example galaxies from the SAMI Galaxy Survey seen in Figs 9 and 10 are good examples of such galaxies. An inability to model these complex structures can lead to two potential problems:

(i) The galaxy substructure can be underfit. This can lead to the substructure systematically driving the estimates in indeterminate directions. Underfitting also leads to underestimates of uncertainties (Taranu et al. 2017).

(ii) Beam smearing is driven by the smearing of the underlying flux profile. If the underlying flux profile is clumpy it can lead to irregular kinematic profiles as seen in our examples in Figs 8 and 10. As such, to get a full understanding of the effects of beam smearing, adequately modelling the gas substructure is important.

We also note that simplifications exist in our current methodology. In particular, assuming the kinematics follow radial profiles is likely to be too simplistic to model a large sample of galaxies. Also, modelling the gas substructure as a hierarchical Gaussian mixture model is also imperfect. We understand that this could lead to similar problems as above.

The above reasoning led to the introduction of the additional σ_0 noise term. This term should help account for simple systematic noise between the model and data.

Also the flexibility of using a hierarchical Gaussian mixture model does provide much better fits to the data. To formalize this we performed a Bayesian model comparison between our current methodology with varying number of blobs and setting $N = 1$. Setting $N = 1$ is similar to a single-component disc model assuming a Gaussian flux profile. In both cases, we calculated the evidence (Z) using DNEST4. Assuming no prior preference for either model, the odds ratio for our current methodology ($\boldsymbol{M}$) compared to a single component model ($\boldsymbol{M}_0$) is given by $O = p(\boldsymbol{D}|\boldsymbol{M})/p(\boldsymbol{D}|\boldsymbol{M}_0) = Z/Z_0$. We found $\log(Z/Z_0) = 1.9 \pm 1.2 \times 10^4$ with $\log(Z/Z_0) > 0$ for all galaxies in our sample from the SAMI Galaxy Survey. Therefore, the variable blob model is preferred compared the single Gaussian component flux model using this measure.

5.2 Effects of beam smearing on kinematic asymmetries

We showed that a toy model with an asymmetric flux distribution, a radial velocity profile, and constant velocity dispersion leads to

asymmetries in the velocity dispersion profile once convolved by the PSF (see Section 3.2). We also saw that modelling of asymmetries in the velocity dispersion profiles of GAMA 30890 can be partially performed by using a flexible gas distribution with radial kinematic profiles plus beam smearing. These observations have implications for the study of asymmetries in observed galaxies.

For example, a popular field of analysis is to estimate the kinematic asymmetries observed in the 2D maps (Shapiro et al. 2008). Analysis of kinematic asymmetries and their drivers have been performed on the SAMI Galaxy Survey previously (Bloom et al. 2017a,b, 2018). In those studies they used KINEMETRY (Krajnović et al. 2006) to estimate the asymmetries in the 2D kinematic maps. KINEMETRY constructs kinematic maps by interpolating between a series of ellipses. Each ellipse is decomposed into a Fourier series of the form,

$$K(a, \psi) = A_0(a) + \sum_{n=1}^{N} (A_n(a) \sin(n\psi) + B_n(a) \cos(n\psi)), \quad (29)$$

where a is the semimajor axis length and ψ is the azimuthal angle. This is usually manipulated to the form,

$$K(a, \psi) = A_0(a) + \sum_{n=1}^{N} k_n(a) \cos(n(\psi - \phi_n(a))), \quad (30)$$

where

$$k_n = \sqrt{A_n^2 + B_n^2} \text{ and } \phi_n = \arctan\left(\frac{A_n}{B_n}\right). \quad (31)$$

For n is odd, the contribution to the 2D map is an even functional contribution. Similarly, for n is even, the contribution is an odd functional contribution. The asymmetric contribution to a kinematic moment per spaxel is typically calculated using a ratio of the sum of $k_{n,\mathrm{mom}}$ for $n > 1$ compared to the first-order velocity moment $k_{1,v}$. In previous works on data from the SAMI Galaxy Survey, the following has been used,

$$v_{\mathrm{asym}} = \frac{k_{3,v} + k_{5,v}}{2k_{1,v}} \text{ and } \sigma_{v,\mathrm{asym}} = \frac{k_{2,\sigma_v} + k_{4,v}}{2k_{1,v}}. \quad (32)$$

The odd moments were ignored for v_{asym} and the even moments were ignored for σ_{asym} as they were estimated to be negligible.

Analysing a sample of 360 galaxies, Bloom et al. (2017a) estimated the mean asymmetry across the FoV to be $\bar{v}_{\mathrm{asym}} = 0.044^{+0.044}_{-0.017}$ and $\bar{\sigma}_{v,\mathrm{asym}} = 0.10^{+0.17}_{-0.04}$. This suggests greater asymmetries in the velocity dispersion compared to the velocity maps. However, the effect of beam smearing on the kinematic asymmetries has not been investigated.

Expanding our method to account for asymmetries in the velocity and velocity dispersion profiles would allow for simultaneous fitting of the kinematic asymmetries while taking into account the effects of beam smearing. This could be achieved by adopting the Fourier series decomposition of the moments similar to KINEMETRY. A natural way to do so would be to parametrize k_n and ϕ_n as radial functions across the disc.

We also note that Bloom et al. (2017a) assigned 23 ± 7 per cent of 360 galaxies from the SAMI Galaxy Survey as perturbed. In their analysis, they assigned galaxies to be perturbed when $\bar{v}_{\mathrm{asym}} > 0.065$. Thus, accounting for asymmetries is an important factor in accurately modelling a larger sample of galaxies at similar resolutions to the SAMI Galaxy Survey.

5.3 Implications for the study of gas turbulence within galaxies

Observations have established that galaxies at $z > 1$ exhibit higher velocity dispersion as well as clumpier gas and velocity dispersion profiles (Genzel et al. 2011; Wisnioski et al. 2011) compared to local galaxies. As the PSF width relative to the observed galaxy size is greater at higher redshift, the effects of beam smearing will typically be greater. As such, it is possible to mistakenly draw correlations across epochs if the effects of beam smearing on the gas velocity dispersion have not been corrected.

One relevant claim has been that star formation feedback processes play an important role as a driver of gas turbulence across epochs (Green et al. 2010, 2014). In contrast, there have been several studies of the localized star formation rate and gas turbulence in nearby galaxies which have not found a significant correlation (Varidel et al. 2016; Zhou et al. 2017). Another recent claim has been that gas turbulence may be driven by the interaction between clumps and the interstellar medium (Oliva-Altamirano et al. 2018). Inferring these relationships requires an ability to accurately determine the intrinsic gas distribution and kinematics. In such studies, our approach would provide a measure for the intrinsic velocity dispersion while taking into account the potentially complex gas distribution.

In particular, inferring relationships between gas clumps and the local kinematics should be much easier in our approach. For example, the study of the residuals in the velocity dispersion map could indicate clear peaks in the velocity dispersion that are correlated with the intrinsic gas distribution. A more natural way within the Bayesian framework, would be to parametrize the velocity dispersion as a function of the gas flux. The simplest approach would be to assume a velocity dispersion component of the form $\log(\sigma_v) \propto F(x, y)$, where the proportionality constant would be a free parameter.

5.4 Potential applications for the study of gas outflows

Gas outflows play an important role as a star formation feedback mechanism (Elmegreen 2009; Federrath et al. 2017a). As such, the identification of gas outflows in star-forming galaxies has received considerable attention (e.g. Ho et al. 2014).

A difficulty in studying gas outflows is to distinguish between the gas rotation, gas outflows, and contributions of beam smearing on the observed emission line profiles. We suggest that applications of forward fitting modelling approaches, such as BLOBBY3D, are ideal to study these galaxies as the rotation and beam smearing contributions can be taken into account simultaneously.

In ideal circumstances, it will be possible to identify outflows as residuals from the 3D model. However, an ideal extension to BLOBBY3D for the study of gas outflows, would be to construct a parametric model for the gas outflows. This parametrization would need to be carefully constructed as winds do not follow the rotational gas kinematics. As such, gas outflows would introduce asymmetries in the emission line profiles with different geometries to the galaxy plane.

This may require the introduction of higher order moments for the emission line profiles. Functional forms for the emission lines that could be used are skewed Gaussian or Hermite–Gaussian profiles. An alternative approach would be to add a secondary gas velocity and velocity dispersion profile which has characteristics that represent an outflow. A simplistic model would likely require a parametrization for the gas component moving radially outwards

in a cone-like shape with a given velocity and velocity dispersion profile.

5.5 A note on run time

Other 3D fitting algorithms take $\mathcal{O}$(seconds – minutes) to run a typical SAMI Galaxy Survey sized cube cut around the H α emission line. The current C++ implementation of BLOBBY3D took the equivalent of ∼450 Central Processing Unit (CPU) hours for a single galaxy within our SAMI Galaxy Survey sample. Wall time was reduced significantly by running DNEST4 in multithreaded mode.

The run time is a function of the complexity of the gas substructure, the signal-to-noise, and the number of samples saved. The run time is a considerable disadvantage for researchers that have very large data sets or are low in computing resources. We have been able to work around this issue by using the Artemis cluster provided by The University of Sydney HPC Service. This gave us access to a large number of cores, such that we could run our methodology for several galaxies simultaneously.

The bottleneck is primarily driven by the number of blobs required to construct the flux profile. Thus decreasing the maximum number of blobs ($N_{\rm max}$) will decrease the run time significantly. Of course, this will lead to posterior distributions for N being abruptly cut-off at $N_{\rm max}$ for some galaxies. We could also implement non-uniform priors for the number of blobs. Similarly, some researchers may find that decomposing the gas distribution into a fixed number of blobs will be adequate to model the gas substructure. In these cases, the prior space will be significantly decreased, and thus will result in significantly faster convergence. We have not explored these possibilities in this work, but it may be important as we scale the methodology to larger samples.

Another approach would be to use an optimization routine compared to a sampling algorithm. In this case, the user would only get an optimized point estimate, but such algorithms are typically much quicker. We note that there is an ability to optimize using DNEST4. We have avoided optimization techniques as we prefer to perform the full inference in order to estimate uncertainties.

Despite the improvements in speed that could be made, we still expect that our method will be significantly slower than other similar 3D fitting algorithms. However, the time restrictions implicit in our method are offset by the improvements in modelling the complex gas substructure that is apparent in typical IFS observations. Furthermore, due to the effects on kinematics that were discussed in Section 5.2, we suggest that researchers should consider using such flexible modelling approaches for the gas substructure in order to accurately infer the intrinsic gas kinematics in their observations.

6 CONCLUSIONS

Beam smearing occurs due to the flux profile being spread-out across the FoV by the seeing. For rotating discs this has significant effects on the observed kinematics. It has been well known that the observed LoS velocity profiles are typically flattened and the LoS velocity dispersion is increased when assuming single flux component galaxy models (Davies et al. 2011).

However, the observed gas distribution often exhibits complex structure including clumps, rings, or spiral arms. Considering this fact, we developed a methodology referred to as BLOBBY3D. BLOBBY3D can model complex gas substructure by using a hierarchical Gaussian mixture model. The kinematics are modelled assuming radial profiles. We take into account the effect of beam smearing by convolving the model by the seeing per spectral slice before comparing it to the data.

BLOBBY3D was applied to a sample of 20 star-forming galaxies from the SAMI Galaxy Survey. We estimated the global gas velocity dispersions for all galaxies in the range $\bar{\sigma}_v \sim$[7, 30] km s^{-1}. This is in comparison to estimates using a single Gaussian component per spaxel that were in the range $\bar{\sigma}_v \sim$[10, 45] km s^{-1}. The relative corrections per galaxy were $\Delta\sigma_v/\sigma_v = -0.29 \pm 0.18$. This has implications for galaxies observed at $z > 1$ that have observed gas velocity dispersions typically much greater than nearby galaxies.

We also show that resolving the gas substructure is important as the gas substructure can lead to asymmetries in the kinematic profiles. A toy model was constructed with asymmetric gas substructure with radial kinematic profiles plus beam smearing to show that asymmetric substructure was observable in the observed gas velocity dispersion. We also found that asymmetries in the velocity dispersion maps for GAMA 30890 can be partially recovered using our methodology, which only introduces asymmetries in the gas distribution. This implies that studies of asymmetries within galaxies should consider the effects of beam smearing on their results.

To accurately infer the intrinsic gas kinematics both the gas flux and kinematic profiles plus beam smearing should be considered. With this in mind, methods such as BLOBBY3D, that are capable of performing such inferences should be an important step in analysing the kinematics for IFS observations of gas discs.

ACKNOWLEDGEMENTS

The SAMI Galaxy Survey is based on observations made at the Anglo-Australian Telescope. The Sydney-AAO Multi-object Integral Field spectrograph (SAMI) was developed jointly by the University of Sydney and the Australian Astronomical Observatory. The SAMI input catalogue is based on data taken from the Sloan Digital Sky Survey, the GAMA Survey, and the VST ATLAS Survey. The SAMI Galaxy Survey is supported by the Australian Research Council Centre of Excellence for All Sky Astrophysics in 3 Dimensions (ASTRO 3D), through project number CE170100013, the Australian Research Council Centre of Excellence for All-sky Astrophysics (CAASTRO), through project number CE110001020, and other participating institutions. The SAMI Galaxy Survey website is http://sami-survey.org/.

The authors acknowledge the University of Sydney HPC service at The University of Sydney for providing HPC and database resources that have contributed to the research results reported within this paper. URL: http://sydney.edu.au/research_support/ BJB acknowledges funding from New Zealand taxpayers via the Marsden Fund of the Royal Society of New Zealand. JBH is supported by an ARC Laureate Fellowship that funds JvdS and an ARC Federation Fellowship that funded the SAMI prototype. EDT acknowledges the support of the Australian Research Council (ARC) through grant DP160100723. JJB acknowledges support of an Australian Research Council Future Fellowship (FT180100231). CF acknowledges funding provided by the Australian Research Council (Discovery Projects DP170100603 and Future Fellowship FT180100495), and the Australia-Germany Joint Research Cooperation Scheme (UA-DAAD). BG is the recipient of an Australian Research Council Future Fellowship (FT140101202). Support for AMM is provided by NASA through Hubble Fellowship grant #*HST*-HF2-51377 awarded by the Space Telescope Science Institute, which is operated by the Association of Universities for

Research in Astronomy, Inc., for NASA, under contract NAS5-26555. MSO acknowledges the funding support from the Australian Research Council through a Future Fellowship (FT140100255). NS acknowledges support of a University of Sydney Postdoctoral Research Fellowship.

REFERENCES

Aumer M., Burkert A., Johansson P. H., Genzel R., 2010, ApJ, 719, 1230
Bekiaris G., Glazebrook K., Fluke C. J., Abraham R., 2016, MNRAS, 455, 754
Bland-Hawthorn J. et al., 2011, Opt. Express, 19, 2649
Bloom J. V. et al., 2017a, MNRAS, 465, 123
Bloom J. V. et al., 2017b, MNRAS, 472, 1809
Bloom J. V. et al., 2018, MNRAS, 476, 2339
Bouché N., Carfantan H., Schroetter I., Michel-Dansac L., Contini T., 2015, AJ, 150, 92
Bournaud F., Elmegreen B. G., Martig M., 2009, ApJ, 707, L1
Bournaud F., Elmegreen B. G., Teyssier R., Block D. L., Puerari I., 2010, MNRAS, 409, 1088
Brewer B., Foreman-Mackey D., 2018, J. Stat. Softw., 86, 1
Brewer B. J., 2014, preprint (arXiv:1411.3921)
Brewer B. J., Pártay L. B., Csányi G., 2011a, Stat. Comput., 21, 649
Brewer B. J., Lewis G. F., Belokurov V., Irwin M. J., Bridges T. J., Evans N. W., 2011b, MNRAS, 412, 2521
Brewer B. J., Foreman-Mackey D., Hogg D. W., 2013, AJ, 146, 7
Brewer B. J., Huijser D., Lewis G. F., 2016, MNRAS, 455, 1819
Bryant J. J., Bland-Hawthorn J., Fogarty L. M. R., Lawrence J. S., Croom S. M., 2014, MNRAS, 438, 869
Bryant J. J. et al., 2015, MNRAS, 447, 2857
Cappellari M., Emsellem E., 2004, PASP, 116, 138
Ceverino D., Dekel A., Bournaud F., 2010, MNRAS, 404, 2151
Cid Fernandes R., Stasińska G., Mateus A., Vale Asari N., 2011, MNRAS, 413, 1687
Contini T. et al., 2016, A&A, 591, A49
Courteau S., 1997, AJ, 114, 2402
Croom S. M. et al., 2012, MNRAS, 421, 872
Davies R. et al., 2011, ApJ, 741, 69
Dekel A. et al., 2009a, Nature, 457, 451
Dekel A., Sari R., Ceverino D., 2009b, ApJ, 703, 785
Di Teodoro E. M., Fraternali F., 2015, MNRAS, 451, 3021
Di Teodoro E. M., Fraternali F., Miller S. H., 2016, A&A, 594, A77
Di Teodoro E. M. et al., 2018, MNRAS, 476, 804
Dobbs C. L., Bonnell I. A., 2007, MNRAS, 374, 1115
Driver S. P. et al., 2011, MNRAS, 413, 971
Elmegreen B. G., 2009, in Andersen J., Nordströaram B., Bland- Hawthorn J., eds, Proc. IAU Symp. 254, The Galaxy Disk in Cosmological Context. Cambridge Univ. Press, Cambridge, p. 289
Epinat B., Amram P., Balkowski C., Marcelin M., 2010, MNRAS, 401, 2113
Federrath C. et al., 2017a, in Crocker R. M., Longmore S. N., Bicknell G. V., eds, Proc. IAU Symp. 322, The Multi-Messenger Astrophysics of the Galactic Centre. Cambridge Univ. Press, Cambridge, p. 123
Federrath C. et al., 2017b, MNRAS, 468, 3965
Förster Schreiber N. M. et al., 2009, ApJ, 706, 1364
Genzel R. et al., 2006, Nature, 442, 786
Genzel R. et al., 2011, ApJ, 733, 101
Glazebrook K., 2013, Publ. Astron. Soc. Aust., 30, e056
Green A. W. et al., 2010, Nature, 467, 684
Green A. W. et al., 2014, MNRAS, 437, 1070
Ho I. T. et al., 2014, MNRAS, 444, 3894
Ho I.-T. et al., 2016, Ap&SS, 361, 280
Iorio G., Fraternali F., Nipoti C., Di Teodoro E., Read J. I., Battaglia G., 2017, MNRAS, 466, 4159
Johnson H. L. et al., 2018, MNRAS, 474, 5076
Kauffmann G. et al., 2003, MNRAS, 346, 1055
Kelvin L. S. et al., 2012, MNRAS, 421, 1007
Krajnović D., Cappellari M., de Zeeuw P. T., Copin Y., 2006, MNRAS, 366, 787
Law D. R., Steidel C. C., Erb D. K., Larkin J. E., Pettini M., Shapley A. E., Wright S. A., 2007, ApJ, 669, 929
Oliva-Altamirano P., Fisher D. B., Glazebrook K., Wisnioski E., Bekiaris G., Bassett R., Obreschkow D., Abraham R., 2018, MNRAS, 474, 522
Persic M., Salucci P., Stel F., 1996, MNRAS, 281, 27
Richards S. N. et al., 2014, MNRAS, 445, 1104
Scott N. et al., 2018, MNRAS, 481, 2299
Shapiro K. L. et al., 2008, ApJ, 682, 231
Sharp R. et al., 2006, in McLean I. S., Iye M., eds, Proc. SPIE Conf. Ser. Vol. 6269, Ground-based and Airborne Instrumentation for Astronomy. SPIE, Bellingham, p. 62690G
Sicking F. J., 1997, PhD thesis, University of Groningen
Skilling J., 2004, in Fischer R., Preuss R., Toussaint U. V., eds, AIP Conf. Proc. Vol. 735, Bayesian Inference and Maximum Entropy Methods in Science and Engineering. Am. Inst. Phys., New York, p. 395
Suyu S. H., Marshall P. J., Hobson M. P., Blandford R. D., 2006, MNRAS, 371, 983
Tamburro D., Rix H. W., Leroy A. K., Mac Low M. M., Walter F., Kennicutt R. C., Brinks E., de Blok W. J. G., 2009, AJ, 137, 4424
Taranu D. S. et al., 2017, ApJ, 850, 70
van de Sande J. et al., 2017, ApJ, 835, 104
van der Hulst J. M., Terlouw J. P., Begeman K. G., Zwitser W., Roelfsema P. R., 1992, in Worrall D. M., Biemesderfer C., Barnes J., eds, ASP Conf. Ser. Vol. 25, Astronomical Data Analysis Software and Systems I. Astron. Soc. Pac., San Francisco, p. 131
Varidel M., Pracy M., Croom S., Owers M. S., Sadler E., 2016, PASA, 33, e006
Walmswell J. J., Eldridge J. J., Brewer B. J., Tout C. A., 2013, MNRAS, 435, 2171
Wisnioski E. et al., 2011, MNRAS, 417, 2601
Zhou L. et al., 2017, MNRAS, 470, 4573

[1]*Sydney Institute for Astronomy (SIfA), School of Physics, A28, The University of Sydney, NSW 2006, Australia*
[2]*ARC Centre of Excellence for All-Sky Astrophysics (CAASTRO)*
[3]*ARC Centre of Excellence for All Sky Astrophysics in 3 Dimensions (ASTRO 3D)*
[4]*Department of Statistics, The University of Auckland, Private Bag 92019, Auckland 1142, New Zealand*
[5]*Research School of Astronomy and Astrophysics, Australian National University, Canberra, ACT 2611, Australia*
[6]*Australian Astronomical Optics, AAO-USydney, School of Physics, University of Sydney, NSW 2006, Australia*
[7]*Centre for Astrophysics and Supercomputing, Swinburne University of Technology, PO Box 218, Hawthorn, VIC 3122, Australia*
[8]*Australian Astronomical Observatory, 105 Delhi Road, North Ryde, NSW 2113, Australia*
[9]*Australian Astronomical Optics, Faculty of Science and Engineering, Macquarie University, 105 Delhi Road, North Ryde, NSW 2113, Australia*
[10]*Department of Physics and Astronomy, Macquarie University, Macquarie, NSW 2109, Australia*
[11]*Ritter Astrophysical Research Center, University of Toledo, Toledo, OH 43606, USA*
[12]*Astronomy, Astrophysics and Astrophotonics Research Centre, Macquarie University, Sydney, NSW 2109, Australia*
[13]*SOFIA Science Center, USRA, NASA Ames Research Center, Building N232, M/S 232-12, PO Box 1, Moffett Field, CA 94035-0001, USA*
[14]*Centre for Translational Data Science, University of Sydney, Darlington, NSW 2008, Australia*
[15]*International Centre for Radio Astronomy Research, University of Western Australia, 35 Stirling Highway, Crawley, WA 6009, Australia*
[16]*Department of Astrophysical Sciences, Princeton University, 4 Ivy Lane, Princeton, NJ 08544, USA*

This paper has been typeset from a TEX/LATEX file prepared by the author.